

# CarBench: A Comprehensive Benchmark for Neural Surrogates on High-Fidelity 3D Car Aerodynamics

Mohamed Elrefaie<sup>1,2,\*</sup>, Dule Shu<sup>3</sup>, Matt Klenk<sup>3</sup>, and Faez Ahmed<sup>1,2</sup>

<sup>1</sup>Department of Mechanical Engineering, Massachusetts Institute of Technology, Cambridge, MA, USA

<sup>2</sup>Schwarzman College of Computing, Massachusetts Institute of Technology, Cambridge, MA, USA

<sup>3</sup>Future Product Innovation, Toyota Research Institute, Los Altos, CA, USA

\*Corresponding Author: mohamed.elrefaie@mit.edu

## ABSTRACT

Benchmarking has been the cornerstone of progress in computer vision, natural language processing, and the broader deep learning domain, driving algorithmic innovation through standardized datasets and reproducible evaluation protocols. The growing availability of large-scale Computational Fluid Dynamics (CFD) datasets has opened new opportunities for applying machine learning to aerodynamic and engineering design. Yet, despite this progress, there exists no standardized benchmark for large-scale numerical simulations in engineering design, making it difficult to evaluate and compare models systematically. In this work, we introduce CarBench, the first comprehensive benchmark dedicated to large-scale 3D car aerodynamics, performing a large-scale evaluation of state-of-the-art models on DrivAerNet++, the largest public dataset for automotive aerodynamics, containing over 8,000 high-fidelity car simulations. We assess eleven representative architectures spanning multiple modeling paradigms: neural operator methods (e.g., Fourier Neural Operator), geometric deep learning approaches (PointNet, RegDGCNN, PointMAE, PointTransformer), transformer-based neural solvers (Transolver, Transolver++, AB-UPT), and implicit field networks leveraging triplane representations (TripNet). Beyond standard interpolation tasks, we perform cross-category experiments in which representative transformer-based solvers trained on a single car archetype are evaluated on unseen categories to probe generalization. Our analysis covers predictive accuracy, physical consistency, computational efficiency, and statistical uncertainty in evaluation metrics, providing a unified comparison across modeling families and quantifying the robustness of performance estimates under shifts in test geometry distributions. To accelerate progress in data-driven engineering, we open-source the complete benchmark framework, including training pipelines, metric-level uncertainty estimation routines based on bootstrap resampling, and pretrained model weights, establishing the first reproducible foundation for large-scale learning from high-fidelity CFD simulations, available at <https://github.com/Mohamedelrefaie/CarBench>.

## Introduction

Standardized benchmarks have played a pivotal role in advancing computer vision, natural language processing, and deep learning at large, enabling fair comparison, reproducibility, and accelerated innovation across tasks and model families. In computer vision, the ImageNet benchmark<sup>1</sup> enabled systematic evaluation at scale and catalyzed key breakthroughs such as AlexNet<sup>2</sup>, a convolutional neural network that significantly outperformed previous methods and popularized deep learning for image classification. Similarly, in natural language processing, benchmarks like GLUE<sup>3</sup>, SuperGLUE<sup>4</sup>, and MMLU<sup>5</sup> supported the development of increasingly capable language models, including BERT<sup>6</sup> and GPT-3<sup>7</sup>, which established state-of-the-art performance across a range of understanding and reasoning tasks. These shared benchmarks help align evaluation practices and support incremental progress across diverse model families and applications.

In contrast, machine learning for computational design and numerical simulations remains fragmented and lacks a unified framework for quantitative comparison. While deep neural networks have shown great promise in accelerating computational fluid dynamics (CFD) simulations and enabling data-driven aerodynamic design<sup>8-14</sup>, the field still lacks a reproducible benchmark that can evaluate models systematically across architectures, geometries, and flow regimes. Most existing studies rely on small proprietary datasets<sup>15,16</sup> or task-specific preprocessing pipelines, often reporting results that are not directly comparable. Moreover, inconsistencies in evaluation, such as mixing physics-based coefficients ( $C_D$ ,  $C_L$ ) with machine-learning-centric losses (MAE, MSE) across incompatible scales, have made it challenging to measure genuine algorithmic progress or generalization to unseen geometries. Recent open datasets such as DrivAerML<sup>17</sup>, AhmedML<sup>18</sup>, and SHIFT-SUV<sup>19</sup> represent important steps toward democratizing data-driven CFD-based research. However, their limited geometric diversity and lack of standardized train, validation, and test splits make it difficult to compare models fairly or assess true generalization. Even recent works that utilize subsets of DrivAerNet++<sup>13,20</sup> have focused on narrow tasks or specific car archetypes, leaving the

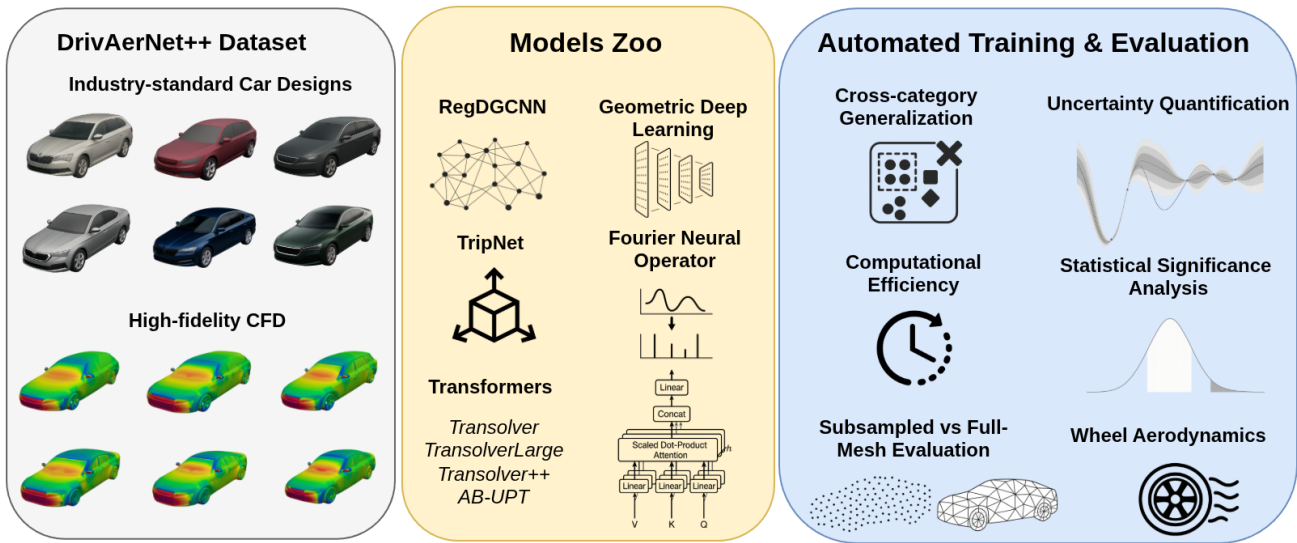


**Figure 1.** Overview of CarBench. The benchmark provides a unified framework for evaluating machine learning models on high-fidelity automotive aerodynamics. It integrates diverse car geometries, CFD-derived surface pressure fields, and automated training pipelines with physics-based and ML metrics. Architectures from multiple model families (GNNs, Geometric Deep Learning, Neural Operators, Transformers, and Triplane networks) are evaluated under a standardized protocol. The framework includes cross-category generalization, uncertainty quantification, computational efficiency analysis, statistical significance evaluation, subsampled vs. full-mesh performance comparison, and wheel aerodynamics prediction. Together, these components enable a comprehensive and physically grounded assessment of aerodynamic surrogate models.

broader question of benchmarking at scale unresolved. Consequently, despite rapid progress in learning-based CFD, there remains no established benchmark comparable to ImageNet or GLUE that unifies data, metrics, and evaluation protocols for the aerodynamic design community. While the benchmark proposed by Tangsali et al.<sup>21</sup> represents an important early step toward standardized AI evaluation in automotive aerodynamics, its scope reflects the constraints of an initial, narrowly focused effort. The study evaluates only three models on a relatively small subset of the DrivAerML dataset, with no assessment of cross-category generalization, uncertainty quantification, or statistical significance. In addition, the test set contains only 48 samples, which makes it difficult to draw statistically meaningful conclusions or assess true generalization performance across diverse geometries. The benchmark also relies on manually defined data splits (90/10) and does not address out-of-distribution testing or full-surface and volumetric flow extrapolation, which limits its usefulness for robust model comparison and real-world deployment. Furthermore, several modern state-of-the-art architectures (e.g., TripNet, Transolver, Transolver++, AB-UPT) are not included, even though Alkin et al.<sup>14</sup> have shown that the models evaluated by Tangsali et al. lag behind contemporary methods by more than an order of magnitude in predictive accuracy.

To fill this gap, we introduce **CarBench**, the first large-scale standardized benchmark for machine learning in aerodynamic design. Built upon the high-fidelity DrivAerNet++ dataset<sup>11</sup>, which encompasses 8,150 steady-state CFD simulations of realistic car geometries, our benchmark provides a rigorous and reproducible platform for evaluating surrogate models under consistent physical and numerical settings. The benchmark defines common data splits, standardized evaluation metrics, and unified training configurations, enabling direct comparison across architectures and learning paradigms. Accurate aerodynamic modeling plays a pivotal role in car design, as small improvements in drag can translate directly into substantial gains in fuel efficiency and electric vehicle range. Among the various components of drag, pressure-induced effects dominate in most passenger cars due to their bluff geometries and large separated wakes. While friction drag can be significant for streamlined configurations, the contribution of pressure drag often exceeds 80–90% of the total aerodynamic resistance<sup>22,23</sup>. Consequently, learning to predict high-fidelity surface pressure fields is not only critical for estimating global aerodynamic coefficients such as  $C_D$  and  $C_L$ , but also for understanding and optimizing flow separation, wake behavior, and overall car performance. In this benchmark, we therefore focus on the task of learning surface-level aerodynamic quantities from geometry, establishing a foundation for scalable, data-driven aerodynamic design.

We comprehensively evaluate eleven state-of-the-art (SOTA) models spanning multiple inductive biases, including neural operator methods such as the Fourier Neural Operator<sup>24</sup>, geometric deep learning architectures such as PointNet<sup>25</sup>, RegDGCNN<sup>26</sup>, PointTransformer<sup>27</sup>, and PointMAE<sup>28</sup>, transformer-based neural solvers such as Transolver<sup>12</sup>, Transolver++<sup>13</sup>, and AB-UPT<sup>14</sup>,

and implicit triplane representations such as TripNet<sup>29</sup>. Our evaluation covers both interpolation and cross-category generalization across distinct car archetypes, including Fastbacks, Notchbacks, and Estatebacks, quantifying predictive accuracy, physical consistency, and computational efficiency on high-resolution aerodynamic surfaces. To promote transparency and community participation, all training pipelines, evaluation scripts, and pretrained model checkpoints are released as open-source resources.<sup>1</sup> An overview of the benchmark framework is shown in Figure 1. It illustrates the full evaluation pipeline, including standardized metrics, multiple architectural families, model-scaling studies, and domain-specific tasks such as wheel-flow prediction. A central component of the framework is the dual-resolution evaluation protocol, which compares model predictions on subsampled surface representations with their corresponding full-resolution CFD surface meshes, enabling a more complete assessment of spatial accuracy. By establishing a reproducible, physics-grounded benchmark for large-scale numerical simulations, CarBench provides a unified foundation for measuring progress in data-driven aerodynamics. It enables fair comparison across models, promotes standardized evaluation practices, and supports future work on generalizable and physically consistent surrogate modeling for engineering design.

In this first release of CarBench, we focus exclusively on steady-state RANS simulations of external automotive aerodynamics and on learning surface pressure fields at a fixed freestream condition from geometry alone. We do not evaluate global aerodynamic coefficients such as drag and lift, volumetric flow fields, or unsteady regimes; these aspects are left as explicit targets for future extensions of the benchmark.

## Results

### Learning Large-scale High-fidelity 3D Car Aerodynamics

**Table 1.** Quantitative comparison on the unseen test set of 1,154 samples across machine learning models, ranked from worst to best by Relative L2 (lower is better). All models are evaluated with batch size 1 on an NVIDIA A100-SXM4-80GB GPU under identical inference settings. Per ISO GUM (Guide to the expression of uncertainty in measurement), uncertainties are rounded to two significant digits and central values are rounded to the same decimal place; precision is standardized per column using the largest uncertainty in that column (MSE (Mean Squared Error): 10, MAE (Mean Absolute Error): 0.01, RMSE (Root Mean Squared Error): 0.1,  $R_{\text{test}}^2$ :  $10^{-4}$ , Rel L2 (Relative L2 Error):  $10^{-4}$ ).

Model	Parameters (M)	Peak Memory (GB)	Mean Latency (ms)	Throughput (sps)	MSE ( $\text{m}^4/\text{s}^4$ )	MAE ( $\text{m}^2/\text{s}^2$ )	RMSE ( $\text{m}^2/\text{s}^2$ )	$R_{\text{test}}^2$	Rel L2
PointNet <sup>25</sup>	1.67	0.29	1.54	648.85	3350 ± 50	31.12 ± 0.170	57.9 ± 0.44	0.7639 ± 0.0027	0.3803 ± 0.0020
NeuralOperator <sup>24</sup>	2.10	0.04	2.14	466.36	2130 ± 47	25.02 ± 0.140	46.2 ± 0.51	0.8503 ± 0.0026	0.3016 ± 0.0019
PointMAE <sup>28</sup>	1.67	0.39	3.11	321.68	1716 ± 39	22.58 ± 0.110	41.4 ± 0.47	0.8791 ± 0.0023	0.2713 ± 0.0016
PointNetLarge <sup>25</sup>	32.58	1.50	8.29	120.65	1384 ± 37	20.51 ± 0.095	37.2 ± 0.50	0.9025 ± 0.0022	0.2436 ± 0.0013
RegDGCNN <sup>26</sup>	1.44	27.11	231.98	4.31	957 ± 50	17.41 ± 0.090	30.9 ± 0.81	0.9327 ± 0.0033	0.2006 ± 0.0016
PointTransformer <sup>27</sup>	3.05	6.65	95.68	10.50	917 ± 82	17.05 ± 0.085	30.3 ± 1.3	0.9359 ± 0.0054	0.1909 ± 0.0024
TripNet <sup>29</sup>	24.10	2.94	15.49	64.52	596 ± 100	13.30 ± 0.090	24.9 ± 2.0	0.9590 ± 0.0067	0.1608 ± 0.0024
Transolver++ <sup>13</sup>	1.81	1.30	28.47	35.12	653 ± 99	13.65 ± 0.085	25.6 ± 1.9	0.9543 ± 0.0066	0.1573 ± 0.0023
Transolver <sup>12</sup>	2.47	1.51	29.84	33.51	605 ± 99	12.75 ± 0.090	24.6 ± 2.0	0.9577 ± 0.0067	0.1503 ± 0.0024
TransolverLarge <sup>12</sup>	7.58	1.68	28.41	35.20	579 ± 100	12.18 ± 0.090	24.1 ± 2.1	0.9595 ± 0.0069	0.1457 ± 0.0025
AB-UPT <sup>14</sup>	6.01	0.27	30.65	32.63	559 ± 160	10.81 ± 0.100	23.6 ± 3.2	0.9675 ± 0.0019	0.1358 ± 0.0024

Table 1 provides a comprehensive quantitative comparison of eleven SOTA machine learning models evaluated on the kinematic surface pressure fields of the DrivAerNet++ dataset. The results reveal a clear performance stratification across model families. Classical point-based networks such as PointNet<sup>25</sup> and PointMAE<sup>28</sup> achieve limited predictive accuracy ( $R_{\text{test}}^2 < 0.88$ , Rel L2  $> 0.27$ ), suggesting that these architectures may be insufficient for capturing the complex spatial patterns present in aerodynamic flows. Their limitations stem from simplified aggregation mechanisms, lower model capacity, and the lack of surface continuity modeling. Geometric and graph-based methods perform significantly better: RegDGCNN<sup>26</sup> achieves a Rel L2 of 0.2006 and  $R_{\text{test}}^2 = 0.933$ , leveraging localized message passing to improve surface-pressure prediction, albeit with substantial computational overhead (27 GB memory, 232 ms inference latency). PointTransformer<sup>27</sup> further reduces the error to Rel L2 = 0.1909 and achieves  $R_{\text{test}}^2 = 0.936$ , demonstrating improved spatial representation at moderate computational cost (6.6 GB).

Transformer-based neural solvers offer the best trade-off between accuracy and efficiency. Both Transolver<sup>12</sup> and Transolver++<sup>13</sup> achieve strong predictive performance ( $R_{\text{test}}^2 \approx 0.95$ ) with compact model sizes (2.5M and 1.8M parameters, respectively) and low inference latency of around 30 ms. The triplane-based TripNet<sup>29</sup> performs comparably ( $R_{\text{test}}^2 = 0.959$ ), though at a higher complexity (24M parameters) and moderate memory cost (2.9 GB). Scaling the transformer architecture improves accuracy further—TransolverLarge reaches a relative error of 0.1457 and an  $R_{\text{test}}^2$  of 0.9595, demonstrating the benefits of increased model capacity. The highest accuracy is achieved by AB-UPT<sup>14</sup>, which sets a new benchmark with  $R_{\text{test}}^2 = 0.9675$

<sup>1</sup>All resources will be made publicly available upon paper acceptance.

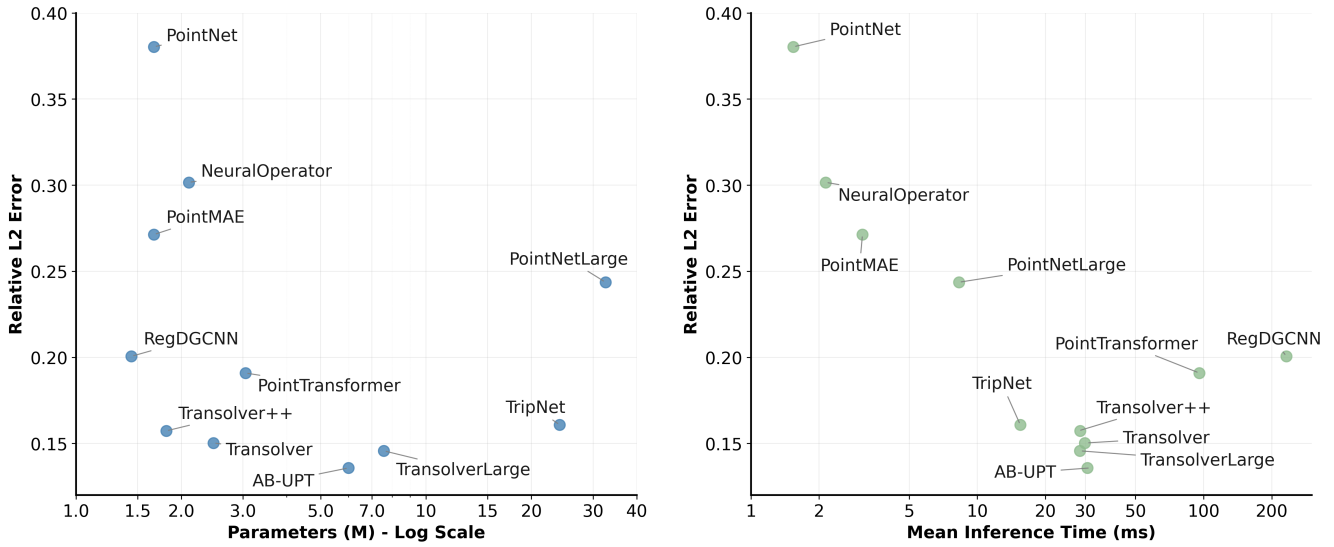
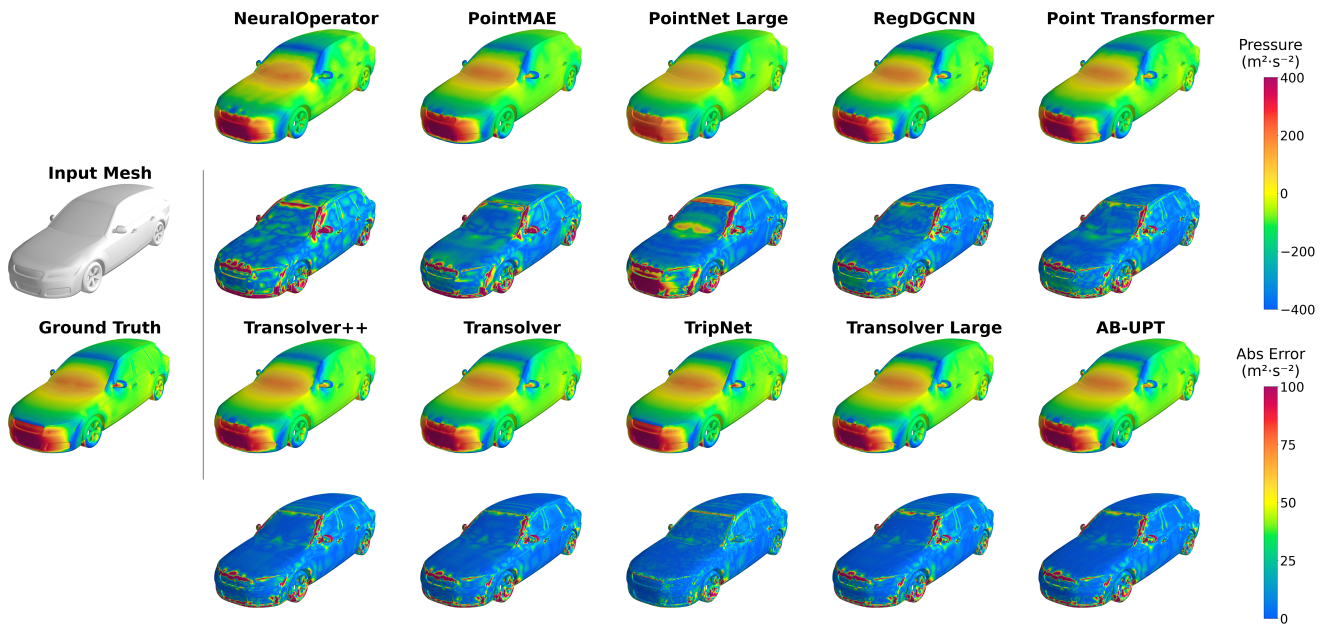


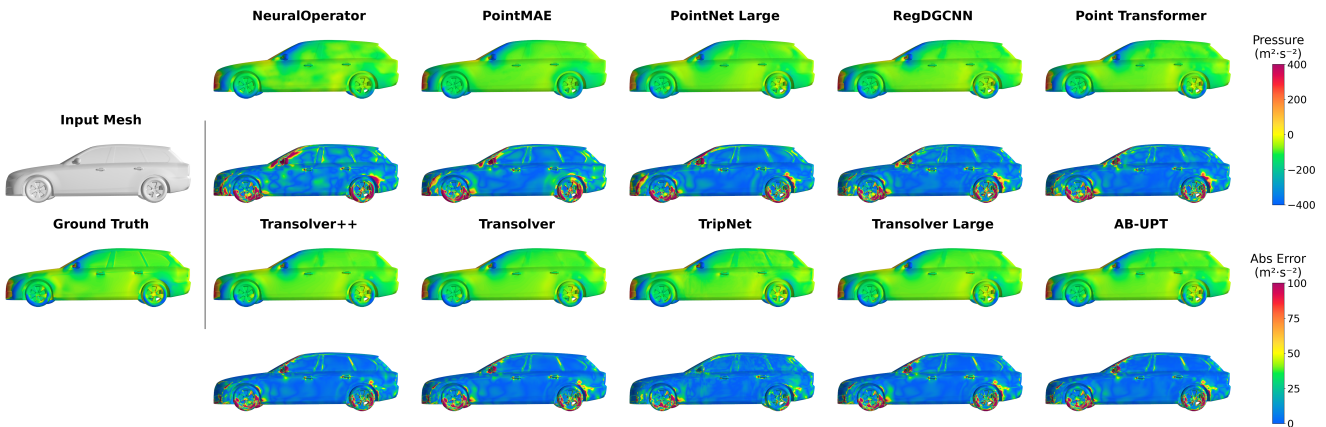
**Figure 2.** Performance–efficiency trade-offs across model families on CarBench. Left: Relative L2 error versus model size (in millions of parameters, log scale). Right: Relative L2 error versus mean inference time (ms) on an NVIDIA A100 GPU. Transformer-based models and implicit-field architectures (AB-UPT, TransolverLarge, Transolver) achieve the best accuracy–efficiency balance, combining low error with compact parameter counts and fast inference. Point-based baselines suffer from higher errors despite lower complexity, while graph-based networks incur large memory and latency overheads. These plots highlight the Pareto frontier of aerodynamic surrogate modeling, revealing models that are both accurate and scalable.

and Rel L2 = 0.1358, along with the lowest mean absolute error ( $10.8 \text{ m}^2/\text{s}^2$ ) and RMSE ( $23.6 \text{ m}^2/\text{s}^2$ ). This improvement is achieved with a moderate model size: AB-UPT contains 6.01M parameters, making it smaller than TransolverLarge (7.6M) and approximately  $2.4\times$  larger than the base Transolver. Despite this intermediate size, AB-UPT remains considerably more parameter-efficient than heavier architectures such as TripNet (24M). Notably, Transolver++ combines strong performance with exceptional compactness, achieving Rel L2 = 0.1573 with the smallest parameter count among the high-performing models. Together, these results confirm that transformer-based and tokenization-aware architectures consistently outperform point-based and graph-based networks in both accuracy and scalability, establishing them as the state-of-the-art for learning high-resolution 3D aerodynamic fields. As illustrated in Figure 2, transformer-based models form a clear Pareto frontier, offering the best balance between predictive accuracy and computational efficiency. Transolver, Transolver++, and AB-UPT all achieve low relative errors (Rel L2 < 0.16) while maintaining compact model sizes under 7M parameters and sub-35 ms inference times. In contrast, networks such as PointNet and PointMAE trade efficiency for accuracy, showing significantly higher errors. TripNet, though accurate, incurs higher memory and parameter costs, while graph-based models like RegDGCNN suffer from long inference times despite strong performance. Overall, transformer-based solvers consistently occupy favorable regions of the accuracy–efficiency landscape, underscoring their suitability for scalable, high-fidelity surrogate modeling in aerodynamic applications.

Figure 3 provides a qualitative comparison of surface pressure predictions for the representative design E\_S\_WW\_WM\_648 from the unseen test set, corresponding to an Estateback configuration with a smooth underbody and open wheels. Transformer-based solvers (Transolver, Transolver++, TransolverLarge, and AB-UPT), together with the implicit-field model (TripNet), produce smooth, physically consistent surface pressure fields that correctly capture high-pressure stagnation zones, surface curvature effects, and pressure recovery along the roof and rear surfaces. In contrast, point-based models introduce localized artifacts, especially near sharp geometric transitions such as the A-pillar, C-pillar, mirrors, and wheel housings. The corresponding error maps further show that AB-UPT, TransolverLarge, and TripNet deliver the most uniform and lowest-magnitude errors across the entire surface geometry, closely matching the CFD ground-truth distribution and demonstrating good robustness to complex surface features. It is worth noting that the error distributions for TransolverLarge and AB-UPT are remarkably similar, likely a result of their shared reliance on point-cloud input representations with identical sampling strategies. In contrast, TripNet operates on triplane-encoded volumetric fields and discretizes the surface mesh differently, which may explain the distinct structure observed in its error map despite achieving similarly low overall error.



(a) Isometric view. Each row compares predicted pressure fields (top) and absolute error maps (bottom) against the CFD ground truth. While all models capture the general pressure distribution, transformer-based architectures exhibit smoother, more physically consistent predictions around the stagnation area and regions with high curvature. TripNet shows the smoothest error map due to its triplane-based volumetric sampling strategy.



(b) Side view. The figure shows predicted pressure fields (top) and absolute error maps (bottom) compared against CFD ground truth. Transformer-based models (TransolverLarge and AB-UPT), together with TripNet, form the top-performing group, maintaining high spatial coherence and capturing high-pressure regions more accurately than other baselines.

**Figure 3.** Qualitative comparison of surface pressure predictions for design E\_S\_WW\_WM\_648 from the unseen test set of the DrivAerNet++ dataset. Both views illustrate model accuracy in predicting detailed aerodynamic pressure fields.

### Wheel Aerodynamics

We further evaluate model performance on the rotating wheel components (Figure 4). In DrivAerNet++, wheels are simulated using a rotating-wall boundary condition that induces realistic surface-pressure gradients arising from tire rotation, rim geometry, and near-ground interactions. The ground is modeled with a moving-wall condition to match the car-relative flow field and ensure physically correct shear behavior in the ground contact region. Wheels can contribute up to 25% of a car’s total aerodynamic drag<sup>30,31</sup>, making them a critical region for assessing local prediction accuracy and capturing high-frequency pressure variations. Unlike prior datasets, DrivAerNet++ includes both open and closed wheel designs as well as smooth and detailed tire geometries, enabling the first standardized evaluation of ML-based aerodynamic prediction on rotating components with diverse geometrical configurations. These components introduce additional geometric complexity and strong three-dimensional pressure gradients, driven by spoke geometry, rim cavities, and tire curvature. Even under steady-state RANS

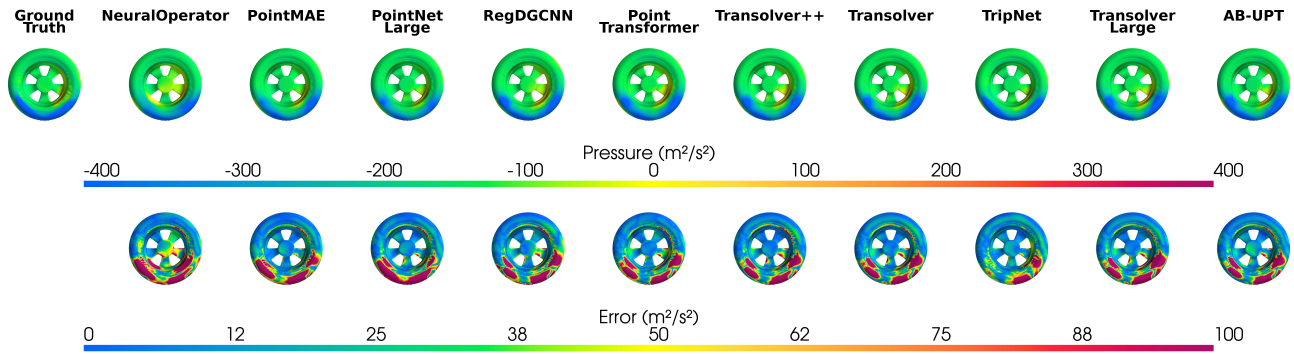


**Figure 4.** Pressure prediction on the front-left wheel compared to the CFD ground truth. Models are ordered from worst (left to right) based on their Relative L2 error. Wheels can contribute up to 25% of a car’s total aerodynamic drag, making accurate pressure modeling around rotating components critical. Compared to prior open-source datasets, DrivAerNet++ uniquely provides detailed and smooth wheel and tire geometries, enabling evaluation across both open and closed wheel configurations.

conditions, these features produce highly localized flow acceleration, separation tendencies, and recirculation pockets around the wheel housing. Such effects create a high-variance prediction regime where surrogate models often struggle to maintain accuracy. By benchmarking model performance in this challenging region, CarBench provides a more rigorous assessment of physical fidelity and model robustness. Transformer-based architectures such as TransolverLarge and AB-UPT achieve the lowest surface-pressure errors, accurately capturing the circumferential pressure distribution and steep gradients around the rim. In contrast, point-based models exhibit localized artifacts and higher sensitivity to small geometric features, highlighting the importance of global attention mechanisms and sufficiently expressive representations for wheel aerodynamics.

### Cross-category Generalization Analysis

**Table 2.** Cross-category generalization performance of Transolver and Transolver++ across combinations of car design categories. Each row corresponds to a training/test category split using the DrivAerNet++ dataset. Models are evaluated in a zero-shot setting, with no fine-tuning or transfer learning on the test category. We report the Relative L2 error (lower is better) and  $R^2_{\text{test}}$  score (higher is better), together with the training and test set sizes and the corresponding train-to-test ratio. These results highlight the models’ ability to extrapolate aerodynamic behavior across distinct vehicle classes under varying data imbalance conditions.

Train categories	Test categories	Rel L2		$R^2_{\text{test}}$		Train size	Test size	Ratio
		Transolver	Transolver++	Transolver	Transolver++			
Fastbacks + Notchbacks	Estatebacks	0.2391	0.2182	0.9088	0.9241	5,376	1,386	3.88
Estatebacks + Fastbacks	Notchbacks	0.1725	0.1729	0.9542	0.9540	5,248	1,403	3.74
Estatebacks + Notchbacks	Fastbacks	0.4894	0.4988	0.6083	0.5933	2,176	5,332	0.41
Estatebacks	Fastbacks + Notchbacks	0.3980	0.4192	0.7446	0.7167	1,024	6,735	0.15
Notchbacks	Estatebacks + Fastbacks	0.4295	0.4483	0.7002	0.6731	1,024	6,718	0.15
Fastbacks	Estatebacks + Notchbacks	0.2539	0.2453	0.8990	0.9057	4,224	2,789	1.51

Generalization to out-of-distribution (OOD) geometries is essential for real-world aerodynamic design, where predictive models must handle unseen vehicle configurations during early-stage development. All conventional passenger vehicles can be categorized into one of three aerodynamic archetypes: Estateback, Notchback, or Fastback, following the classification proposed by Hucho<sup>32</sup>. We conduct cross-category experiments in which models trained on one or more car archetypes are tested on entirely disjoint shape categories. This setup probes whether models learn transferable aerodynamic priors rather than memorizing category-specific geometric cues. To explore generalization under systematically varied training distributions, we focus on Transolver and Transolver++ as representative architectures. Both models offer strong accuracy–efficiency trade-offs, modest parameter counts, and fully open-source training pipelines, making them suitable for repeated retraining across many data splits.<sup>2</sup> Accordingly, cross-category results reported here should be interpreted as characterizing these two representative

<sup>2</sup>In contrast, models such as AB-UPT and TripNet were released only as pretrained checkpoints, which prevents retraining under new data splits.

architectures rather than the entire model zoo. As shown in Table 2, several consistent trends emerge:

**1. Training on the largest and most diverse category yields the strongest generalization.** Fastbacks provide between 4,224 and 5,353 training samples depending on the split, and both models transfer well to Estateback and Notchback categories. For instance, training on Fastbacks alone and testing on Estatebacks + Notchbacks yields Rel L2 = 0.2539 (Transolver) and 0.2453 (Transolver++), among the best zero-shot results in the table. This indicates that the geometric richness of Fastbacks enables the network to learn aerodynamic features that generalize across categories.

**2. Training on small categories leads to poor generalization across all directions.** Estatebacks and Notchbacks each contain only 1,024 samples. When used alone for training, they generalize poorly to the other two categories, with Rel L2 in the range 0.3980–0.4483 and  $R^2_{\text{test}}$  often below 0.72. This degradation highlights that limited geometric variability restricts the model’s ability to extrapolate aerodynamic behavior.

**3. Combining two categories improves generalization, particularly when the overall training set is sufficiently large.** Training on (Fastbacks + Notchbacks) or (Estatebacks + Fastbacks) significantly improves transfer performance. For example:

- Fastbacks + Notchbacks → Estatebacks: Rel L2 = 0.2391 (Transolver)
- Estatebacks + Fastbacks → Notchbacks: Rel L2  $\approx$  0.1725–0.1729, the best cross-category result in the table

These findings demonstrate a strong complementarity effect: adding even a modest number of Estateback or Notchback samples to a large Fastback dataset improves robustness on unseen geometries.

**4. Predicting Fastbacks without Fastback training data is the hardest direction.** Training on Estatebacks + Notchbacks (2,176 samples) and testing on Fastbacks (5,332 samples) results in the worst performance overall, with Rel L2 values around 0.49–0.50. Fastbacks contain curvature patterns, roofline transitions, and wake characteristics that are not present in the Estateback or Notchback geometries, making them fundamentally different from the training distribution. This strong asymmetry is further amplified by the large training-set size available for Fastbacks: models trained on the extensive Fastback subset (5,353 samples) generalize well to the other categories, whereas the much smaller combined Estateback + Notchback training set lacks the geometric diversity necessary for successful zero-shot prediction of Fastbacks.

**5. Dataset size plays a more dominant role than geometric diversity in cross-category generalization.** A comparison of the two asymmetric transfer directions reveals that larger training sets generalize substantially better than smaller but more diverse ones. Training solely on Fastbacks (4,224 samples) yields strong generalization to Estatebacks and Notchbacks, achieving Rel L2 values of 0.2539 and 0.2453. In contrast, training on the more diverse but much smaller Estateback + Notchback set (2,176 samples) results in the poorest overall performance when predicting Fastbacks, with Rel L2 near 0.49–0.50. This indicates that, within the scale of our dataset, the quantity of training examples dominates geometric diversity in determining cross-category generalization. Diversity remains important, but only when supported by sufficient dataset size.

Overall, these results demonstrate that cross-category extrapolation is feasible only when the training distribution spans sufficient geometric diversity and aerodynamic modes. Diverse shape families produce robust, transferable aerodynamic priors, whereas narrow categories lead to systematic failure modes when encountering unseen geometries.

### Computational Efficiency and Performance Trade-offs

The efficiency analysis reveals clear trade-offs between accuracy, runtime, and memory cost (Table 1). NeuralOperator achieves the highest throughput (466 samples/s) and the lowest memory footprint (0.04 GB), but this comes at the expense of predictive accuracy ( $R^2_{\text{test}} = 0.85$ ). In contrast, graph-based models such as RegDGCNN exhibit substantial latency ( $\sim$ 232 ms) and extremely high memory usage (27 GB), reflecting the overhead of dynamic  $k$ -NN graph construction and message passing. Transformer-based architectures strike a far more favorable balance. Both Transolver and Transolver++ operate at 28–30 ms latency with modest memory requirements (1.3–1.5 GB), while TransolverLarge remains similarly efficient (28 ms, 1.68 GB). Implicit field models such as TripNet also exhibit competitive runtime (15 ms) with moderate memory usage (2.94 GB). AB-UPT offers competitive runtime characteristics (31 ms, 0.27 GB) while achieving the best overall accuracy, demonstrating that high predictive fidelity can be attained without incurring excessive computational overhead.

### Subsampled vs. Full-Resolution Mesh Evaluation

A common limitation in prior aerodynamic learning studies is that model accuracy is often reported only on subsampled point clouds or reduced mesh representations<sup>12,13,24,33</sup>, which can obscure real performance at full resolution. In this work, all models are trained on sampled point clouds with 10,000 surface points. To assess robustness beyond training resolution, we evaluate predictions on both this 10,000 subsampled mesh and the full-resolution surface mesh containing 487,846 nodes. As shown in Table 3, point-based models such as PointNet and PointMAE exhibit the highest errors at both scales and degrade more

**Table 3.** Comparison of model performance on subsampled point-cloud evaluations (10,000 surface points) and full-resolution mesh (487,846 surface points) for a representative unseen test sample (E\_S\_WW\_WM\_648). All error metrics are reported in kinematic pressure units ( $\text{m}^2/\text{s}^2$ ). Models are ranked from worst (top) to best (bottom) based on their Relative L2 errors.

Model	MAE ( $\text{m}^2/\text{s}^2$ )		RMSE ( $\text{m}^2/\text{s}^2$ )		Rel L2		$R_{\text{test}}^2$	
	10k	Full	10k	Full	10k	Full	10k	Full
PointNet	32.2	32.5	62.4	63.3	0.395	0.403	0.757	0.747
NeuralOperator	25.9	26.3	51.2	54.4	0.324	0.347	0.837	0.813
PointMAE	23.0	24.7	46.2	52.0	0.292	0.331	0.867	0.829
PointNetLarge	22.0	25.1	42.1	55.3	0.266	0.352	0.890	0.807
RegDGCNN	16.5	19.9	32.4	46.1	0.205	0.293	0.935	0.866
PointTransformer	16.2	20.6	29.5	47.0	0.187	0.299	0.946	0.861
TransolverLarge	12.2	18.5	25.5	47.2	0.161	0.300	0.959	0.860
TripNet	13.6	19.8	25.1	44.0	0.158	0.297	0.961	0.863
Transolver++	12.3	18.3	24.6	46.0	0.156	0.293	0.962	0.867
Transolver	11.7	17.7	23.7	46.1	0.150	0.294	0.965	0.866
AB-UPT	10.2	17.2	21.5	45.7	0.136	0.291	0.971	0.869

sharply at full resolution, reflecting limitations in spatial continuity and high-frequency recovery. PointNetLarge, RegDGCNN, and PointTransformer reduce Rel L2 into the 0.18–0.27 range, achieving smoother pressure fields and higher  $R_{\text{test}}^2$  values (0.89–0.95).

Among implicit and transformer-style solvers, accuracy improves further: TripNet reaches a Rel L2 of 0.158 with  $R_{\text{test}}^2 = 0.961$ , while Transolver++ and TransolverLarge achieve similar accuracy (0.156 and 0.161). Transolver performs even better with a Rel L2 of 0.150 and  $R_{\text{test}}^2 = 0.965$ . The best overall performance is obtained by AB-UPT, which achieves the lowest surface error (Rel L2 = 0.136) and the highest predictive fidelity ( $R_{\text{test}}^2 = 0.971$ ). When predictions are interpolated from the 10,000-point representation to the full-resolution CFD mesh, the error increases across all models, typically by 15–30%, due to the higher geometric complexity and the added interpolation step. Although multi-pass chunked inference could, in principle, mitigate this gap, such approaches introduce inconsistencies across architectures with differing memory limits and input constraints. For fairness and reproducibility, all models are therefore evaluated using the same 10,000-point sampling followed by uniform interpolation to the full CFD surface mesh. This standardized protocol yields a consistent, physically meaningful basis for comparing surrogate aerodynamic models at both reduced and full-resolution levels.

### Statistical Uncertainty of Evaluation Metrics

In this section, the term ‘uncertainty’ refers to statistical uncertainty in aggregate evaluation metrics, rather than predictive uncertainty on individual samples or spatially varying epistemic/aleatoric uncertainty. To rigorously assess the uncertainty in our performance metrics, we apply stratified paired bootstrap resampling<sup>34,35</sup> with  $B = 2000$  replicates. Entire car geometries are resampled with replacement, ensuring that the spatial correlation structure of each surface is preserved. Stratification by car archetype (Estate, Notchback, Fastback) maintains the original category proportions in every bootstrap replicate, which leads to confidence intervals that accurately reflect the geometric and aerodynamic diversity of the test set. Across models, the bootstrap uncertainty in Relative L2 error remains small compared to the mean values, with all confidence intervals lying between  $\pm 0.0013$  and  $\pm 0.0025$ , while the mean Relative L2 spans from 0.1358 to 0.3803. This narrow range means that the ranking by Relative L2 is statistically stable; for example, the gap between AB-UPT ( $0.1358 \pm 0.0024$ ) and TransolverLarge ( $0.1457 \pm 0.0025$ ) is several times larger than their respective uncertainties. Lower performing models such as PointNet and NeuralOperator also show larger spread in absolute metrics, with MSE uncertainties of  $\pm 50$  and  $\pm 47$ , respectively, which is consistent with their higher average error levels. For mid-range models such as RegDGCNN and PointTransformer, RMSE uncertainties of  $\pm 0.81$  and  $\pm 1.3$  indicate moderate variability across the 1,154 test geometries.

In contrast, the strongest models in terms of Relative L2, including TripNet, Transolver, TransolverPlus, TransolverLarge, and AB-UPT, have similar Relative L2 uncertainties in the band  $\pm 0.0023$  to  $\pm 0.0025$ , but their MSE and RMSE intervals are not uniformly small. AB-UPT, for instance, achieves the lowest overall error with Relative L2  $0.1358 \pm 0.0024$  and RMSE  $23.6 \pm 3.2$ , where the RMSE uncertainty is larger than for some weaker models in absolute terms. This pattern reflects the fact that even high-performing models can exhibit noticeable variation on the most challenging geometries, especially those that dominate the tails of the error distribution. There is no clear monotonic relationship between parameter count and uncertainty. TripNet, with 24 million parameters, has RMSE uncertainty of  $\pm 2.0$ , similar to smaller transformer models such as Transolver and TransolverPlus, which lie in the  $\pm 1.9$  to  $\pm 2.0$  range, while AB-UPT with 6.01 million parameters shows the largest RMSE uncertainty of  $\pm 3.2$ . This suggests that architectural design and training procedure influence robustness more than parameter

count alone. Overall, the bootstrap analysis supports that the ranking of models by Relative L2 is statistically reliable, while also revealing that even the best models retain non-negligible variability on complex three-dimensional flows in DrivAerNet++.

### Statistical Significance Analysis

Table 1 reports performance metrics with 95% bootstrap confidence intervals, enabling a robust evaluation of model ranking beyond point estimates. AB-UPT achieves the lowest relative L2 error ( $0.1358 \pm 0.0024$ ) and highest coefficient of determination ( $R_{\text{test}}^2 = 0.9675 \pm 0.0019$ ), with confidence intervals that do not overlap with those of any other model, providing strong statistical evidence of its performance advantage. The next-best model, TransolverLarge, achieves  $\text{Rel L2} = 0.1457 \pm 0.0025$  and  $R_{\text{test}}^2 = 0.9595 \pm 0.0069$ , followed by Transolver ( $0.1503 \pm 0.0024$ ) and Transolver++ ( $0.1573 \pm 0.0023$ ). While TransolverLarge and Transolver show marginal interval overlap near 0.148, suggesting comparable accuracy, both outperform Transolver++ with statistically significant separation in error bounds. In contrast, earlier architectures such as PointTransformer ( $0.1909 \pm 0.0024$ ) and RegDGCNN ( $0.2006 \pm 0.0016$ ) fall well outside the top-performing range, and have intervals that do not intersect with those of the best-performing models. These results confirm that transformer-based models, particularly unified architectures like AB-UPT, offer statistically robust improvements in predictive fidelity over prior methods.

### Statistical Error Distributions and Failure-Case Analysis

Systematically analyzing the worst-performing cases for each model is crucial to identify where the predictions break down and which flow regions, such as high-curvature surfaces, remain most challenging. Such analysis provides valuable insights into model limitations and helps guide future improvements in network architecture and data representation. To provide a detailed assessment of model performance beyond average errors, we report both relative and absolute percentile-based error statistics, which together capture accuracy across typical and extreme flow regions. The *median relative error* measures the scale-invariant deviation between predicted and true surface pressures, offering a normalized indicator of global model accuracy that is independent of absolute pressure magnitude. In contrast, the percentile-based metrics ( $P50$ ,  $P90$ ,  $P95$ , and  $P99$ ) quantify absolute deviations in physical units ( $\text{m}^2/\text{s}^2$ ), providing an interpretable measure of how far predictions deviate from ground truth across the surface. The  $P50$  error represents the median deviation per surface point and reflects the model’s typical predictive fidelity in low- and moderate-gradient regions. The  $P90$  and  $P95$  percentiles capture the upper tail of the error distribution, corresponding to more complex aerodynamic regions such as sharp edges, high-curvature regions, and stagnation zones. Finally, the  $P99$  error measures the rare but large outliers, typically occurring near high-curvature features or sharp discontinuities in the pressure field.

**Table 4.** Statistical error distribution of surface pressure prediction across models, sorted from worst to best according to Median Relative Error. Median relative error is dimensionless, while percentile errors are reported in absolute pressure units ( $\text{m}^2/\text{s}^2$ ). Lower values indicate higher predictive accuracy. Percentiles describe the cumulative distribution of absolute errors across all surface points, capturing both typical and extreme deviations.

Model	Median Rel. Error	P50 Error ( $\text{m}^2/\text{s}^2$ )	P90 Error ( $\text{m}^2/\text{s}^2$ )	P95 Error ( $\text{m}^2/\text{s}^2$ )	P99 Error ( $\text{m}^2/\text{s}^2$ )
PointNet	0.19	17.57	66.04	101.32	249.43
NeuralOperator	0.15	14.36	53.35	82.93	192.86
PointMAE	0.13	13.17	48.44	72.70	167.14
PointNetLarge	0.12	11.10	46.61	72.06	156.91
RegDGCNN	0.10	9.91	37.03	54.15	111.75
PointTransformer	0.10	9.50	34.77	50.40	103.05
Transolver++	0.09	7.99	30.99	44.73	89.25
TripNet	0.08	7.45	29.10	43.20	87.50
Transolver	0.07	6.89	27.96	40.75	83.04
TransolverLarge	0.07	6.84	27.88	40.67	83.17
AB-UPT	0.06	6.20	25.40	37.90	78.30

Table 4 shows a clear progression in accuracy from early point-based models to modern operator-, transformer-, and triplane-based architectures. Classical baselines such as PointNet and NeuralOperator exhibit the highest median relative errors ( $\geq 0.15$ ) and large tail errors ( $P99 > 190 \text{ m}^2/\text{s}^2$ ). Geometric deep networks (RegDGCNN, PointTransformer) substantially reduce both median and high-percentile errors, reflecting improved local feature aggregation. Transformer-style solvers and implicit models achieve the strongest overall performance. Transolver, TransolverLarge, and Transolver++ maintain low median errors (0.07–0.09) with P50 errors below  $8 \text{ m}^2/\text{s}^2$ . TripNet performs similarly, while AB-UPT attains the best results overall, achieving the lowest median error (0.06) and smallest extreme deviations ( $P99 = 78.30 \text{ m}^2/\text{s}^2$ ). These results highlight the benefits of global receptive fields and rich feature parameterizations for accurate and robust surface-pressure prediction.

## Convergence Behavior of Neural Surrogate Models

Learning curves provide essential insight into convergence behavior, generalization, and training stability. Figure 5 shows the training and validation loss trajectories for the representative models in our benchmark. All architectures exhibit smooth and stable convergence without signs of overfitting, demonstrating the effectiveness of the unified training setup, mixed-precision optimization, and early stopping. Lightweight encoder–decoder models such as NeuralOperator and PointMAE converge rapidly within the first 50–80 epochs, though they settle at higher final losses compared to more expressive architectures.

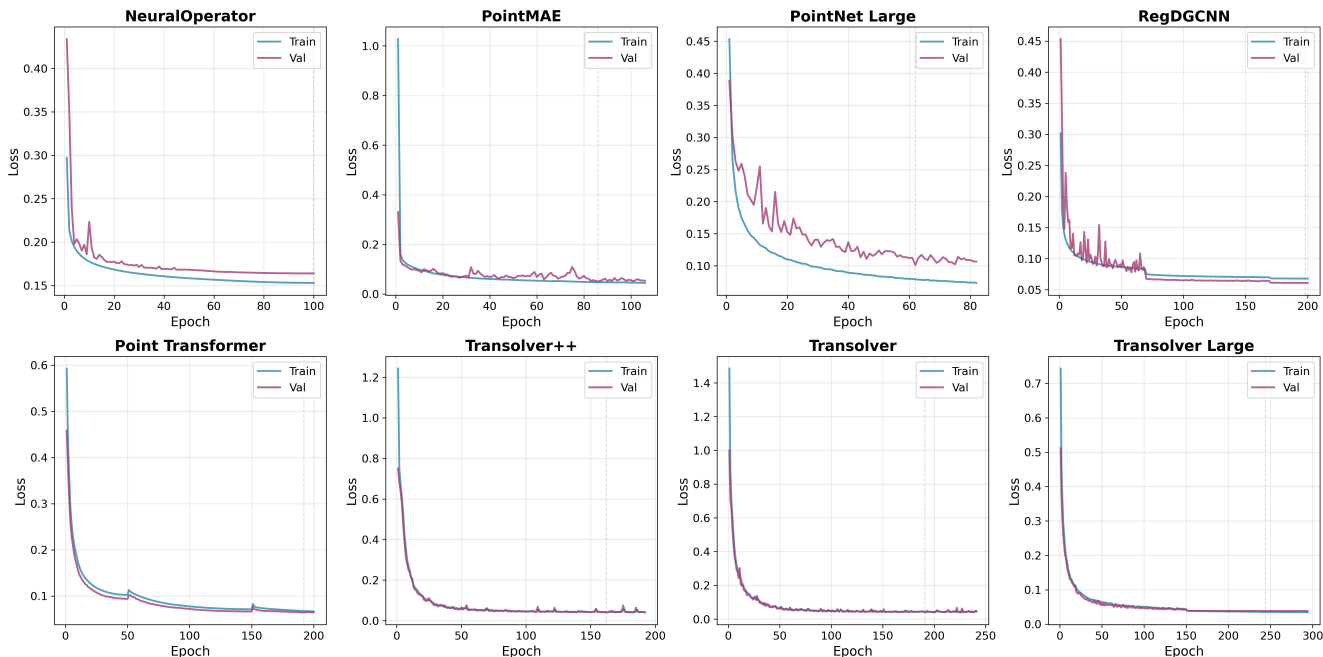


**Figure 5.** Training and validation loss curves for eight models evaluated on the DrivAerNet++ dataset. Each plot shows model convergence behavior over training epochs, with blue indicating training loss and red indicating validation loss. These trends highlight differences in optimization stability and representational efficiency across network architectures for aerodynamic learning.

Attention- and graph-based models, including PointTransformer and RegDGCNN, require longer training horizons but achieve lower and more stable validation losses. Among high-capacity models, Transolver, Transolver++, and TransolverLarge display the smoothest and most consistent optimization behavior, with Transolver++ reaching strong performance particularly quickly. These curves highlight clear trends connecting model capacity, convergence speed, and final accuracy across modern aerodynamic surrogate architectures.

## Discussion

CarBench establishes a comprehensive and physically consistent framework for evaluating machine learning models in aerodynamic prediction. Rather than treating performance solely as a numerical comparison, this benchmark integrates physical interpretability into the evaluation process. All reported quantities are expressed in kinematic units ( $m^2/s^2$ ), ensuring consistency with CFD conventions and allowing direct comparison to physically meaningful scales. By combining predictive accuracy, computational efficiency, and scalability within a unified assessment framework, the benchmark provides a holistic understanding of how different modeling paradigms balance precision, speed, and resource requirements.

A key insight from this work is the critical role of large-scale and diverse training datasets in enabling robust generalization to unseen designs. Cross-category experiments demonstrate that models trained on geometrically rich and varied data exhibit stronger zero-shot performance, confirming that diversity in aerodynamic forms is essential for learning transferable flow representations. Equally important is the choice of evaluation resolution: unlike prior studies that report results only on subsampled point clouds or decimated meshes, CarBench systematically evaluates both subsampled predictions and full-mesh resolution, ensuring that model performance reflects the fidelity of the original high-resolution CFD data. This approach provides a fair and realistic measure of physical accuracy and generalization beyond the limitations of reduced data representations. In addition to numerical evaluation, the benchmark incorporates qualitative visualization and error analysis, revealing the flow

regions where models tend to struggle, such as stagnation regions, high-curvature surfaces, and areas with strong pressure gradients. These visual analyses help identify specific geometric or flow regimes that require denser sampling or model refinement. Finally, the inclusion of component-level evaluations, such as rotating wheel aerodynamics, demonstrates the benchmark’s capacity to test models under detailed boundary conditions and localized flow effects.

Beyond cross-model comparison, we also analyzed the effect of model capacity on performance. We tested two architectures in both their baseline and enlarged configurations: PointNet and Transolver. For PointNet, increasing model size from 1.67M to 32.58M parameters reduced the relative L2 error from 0.3803 to 0.2436, a substantial improvement that highlights the benefit of higher representational capacity for complex aerodynamic surfaces. In contrast, scaling Transolver from 2.47M to 7.58M parameters led to only a modest improvement in relative L2 error—from 0.1503 to 0.1457—representing less than a 1% gain. This suggests diminishing returns at higher capacity levels for already well-performing transformer architectures, and highlights that architectural design and training strategy may be more influential than raw parameter count beyond a certain threshold. These results underscore the importance of balancing model capacity with data efficiency to maximize both physical accuracy and practical utility.

We further investigated different geometric representations. While most models evaluated in this benchmark are point-cloud-based, we also included architectures that leverage alternative spatial encodings. TripNet employs a triplane implicit neural representation that maps the 3D car surface into orthogonal feature planes, enabling dense reconstruction of aerodynamic quantities, whereas RegDGCNN constructs dynamic graphs over sampled point clouds to capture local neighborhood relations and surface connectivity. Our experiments show that for the task of predicting surface pressure distributions, point cloud-based representations, when densely sampled, are highly reliable and faithfully capture the underlying aerodynamic fields on complex car geometries. This finding suggests that high-resolution surface sampling provides sufficient spatial information for accurate flow reconstruction without requiring volumetric representations for steady-state external aerodynamics. Together, these elements establish CarBench as a rigorous, interpretable, and scalable foundation for advancing data-driven research in computational aerodynamics. By promoting standardized, physics-consistent evaluation, this benchmark lays the groundwork for reproducible progress in neural CFD modeling and for the next generation of generalizable, data-driven aerodynamic solvers.

The following key findings summarize the main insights derived from our large-scale evaluation and analysis across architectures, datasets, and geometric representations:

- **Dataset scale and diversity** are essential for generalization. Models trained on large and geometrically varied datasets outperform those trained on narrow distributions, underscoring a core strength of the DrivAerNet++ dataset.
- **Transformer-based models** (e.g., TransolverLarge, Transolver, and AB-UPT) consistently achieve state-of-the-art results, demonstrating strong generalization and physical coherence in pressure field prediction.
- **Evaluation at full mesh resolution** is critical for realism. Reporting performance only on sparse subsamples underrepresents model errors; our framework emphasizes fidelity by comparing against high-resolution CFD ground truth across the entire surface mesh.
- **Model scaling improves accuracy.** Larger variants of PointNet and Transolver significantly reduced relative L2 errors (from 0.38 to 0.24 and from 0.15 to 0.14, respectively), showing that increased capacity enhances physical fidelity.
- **Representation matters.** While implicit triplane and graph-based networks provide complementary strengths, high-resolution point-cloud representations remain highly effective and physically consistent for surface pressure prediction.

## Conclusions

This work introduces a unified, model-agnostic framework for training and evaluating neural surrogates for automotive aerodynamics. Spanning eight car archetypes, thousands of high-fidelity steady RANS simulations, and eleven SOTA deep learning models, CarBench enables reproducible and physics-consistent comparison across diverse architectures while reporting all physical quantities in accordance with CFD conventions. Our standardized pipeline, covering data preprocessing, mixed-precision optimization, early stopping, and a common evaluator, helps ensure that, for models retrained in our framework, measured gains largely reflect architectural differences rather than experimental confounders. Across extensive experiments, transformer-based models emerge as the most accurate and scalable, with AB-UPT and TransolverLarge achieving the highest overall accuracy and Transolver++ offering an especially favorable accuracy–efficiency trade-off. Analyses on full mesh evaluations, rotating wheel aerodynamics, and cross-category generalization highlight three central findings: (i) evaluating at CFD resolution is essential for realistic error accounting, (ii) component-level tests reveal localized failure modes around high curvature and separation zones, and (iii) dataset scale and geometric diversity are decisive for zero-shot generalization to unseen archetypes.

While machine learning applications in industrial aerodynamic design are still in their early stages, it is important to acknowledge that CFD itself provides an approximation of experimental reality. For the DrivAerNet++ dataset, steady-state RANS baselines show deviations below 3% for the Fastback archetype and below 5% for the Estateback and Notchback configurations compared to wind tunnel measurements<sup>11</sup>. Generating the DrivAerNet++ dataset required an immense computational investment of more than three million CPU hours distributed across eight archetypes and more than eight thousand simulations, highlighting the prohibitive cost of large-scale CFD data generation. In contrast, training the benchmarked surrogate models requires less than a few hundred GPU hours per architecture, enabling rapid experimentation and model iteration at a fraction of the cost. Moreover, the cross-category generalization experiments, where models trained on one car archetype were evaluated on unseen categories, demonstrate that scaling such datasets across multiple DrivAerNet++ variants could otherwise require tens or even hundreds of thousands of additional simulations, corresponding to tens of millions of additional core hours. This further emphasizes the necessity of robust and generalizable machine learning surrogates.

The best performing models, AB-UPT and TransolverLarge, achieve relative L2 errors of approximately 13–15%. These discrepancies should therefore be interpreted with care, as they represent compounded sources of error arising from both CFD approximations and the surrogate modeling process. Nevertheless, large-scale datasets based on RANS remain the only practical path toward training machine learning models at the tens or hundreds of thousands of simulation scale required for generalization and foundation modeling. Accordingly, the goal of this benchmark is not merely to replicate CFD but to catalyze the development of more accurate, robust, and physically grounded surrogates that can ultimately bridge the gap between numerical simulation and real-world aerodynamics. We believe that CarBench provides a critical foundation for advancing three-dimensional machine learning for large-scale numerical simulations, promoting fair comparison, reproducibility, and continued progress in data-driven aerodynamic design. While this work focuses on car aerodynamics, the benchmark framework is generalizable to other domains where the objective is to learn flow fields conditioned on 3D geometry. Potential applications include external aerodynamics of aircraft, turbomachinery design, and other geometry-dependent fluid dynamics systems.

In summary, CarBench establishes a rigorous foundation for reproducible, physics-aware benchmarking in neural CFD, clarifies the strengths of modern transformer/operator architectures, and charts a practical path toward generalizable, data-driven aerodynamic solvers for real-world design applications.

## Methods

### DrivAerNet++ Dataset

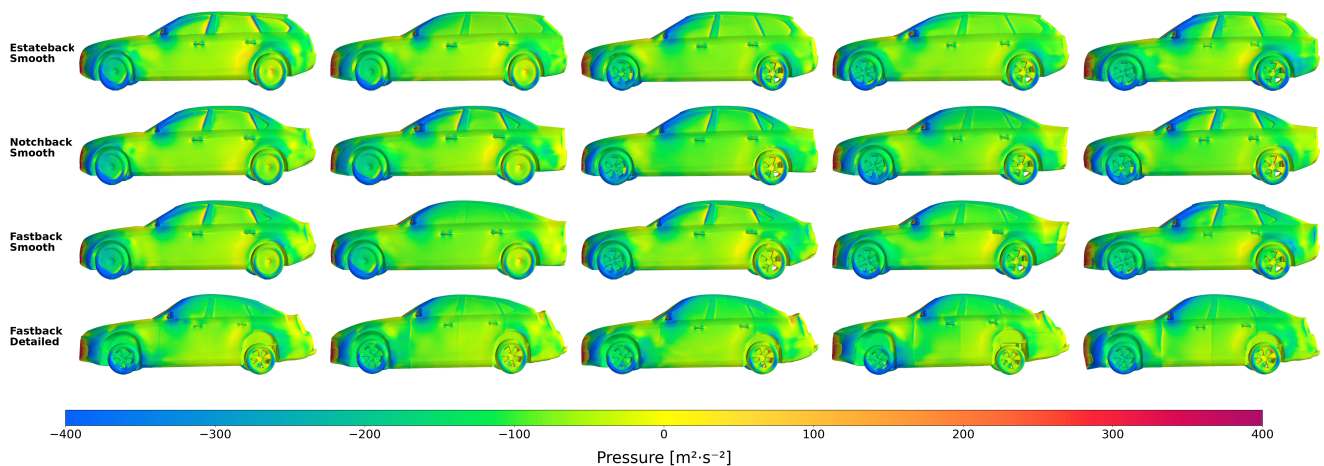


**Figure 6.** Surface pressure distributions for representative designs across different car categories in DrivAerNet++. Rows correspond to Estateback, Notchback, and Fastback archetypes under smooth and detailed configurations. The color scale represents kinematic pressure ( $\text{m}^2/\text{s}^2$ ), highlighting regions of low pressure over the windshield and roof and high pressure near the front bumper and rear stagnation zones. These examples illustrate the geometric and aerodynamic diversity captured in the dataset.

DrivAerNet++ represents a significant advancement in automotive aerodynamics datasets, expanding upon the original DrivAerNet with enhanced geometric diversity and higher-fidelity simulations. The dataset comprises 8,150 parametrically generated car configurations, each representing a physically realistic automotive design within the constraints of modern passenger cars. The scale, fidelity, and multimodal structure of DrivAerNet++ have enabled a range of downstream research

applications. These include *TripOptimizer*<sup>36</sup>, a fully differentiable framework for three-dimensional shape optimization and inverse design; a multi-agent *Design Agents* system<sup>37</sup> that integrates aesthetic and aerodynamic objectives; and surrogate models for accurate prediction of flow fields and aerodynamic coefficients. Collectively, these applications demonstrate the dataset’s role as a foundation for developing and benchmarking advanced methods in data-driven design and scientific machine learning. Representative surface pressure distributions across multiple car archetypes and configurations in the DrivAerNet++ dataset are shown in Figure 6. Distinct aerodynamic behaviors are observed between the Estateback, Notchback, and Fastback designs, as well as between smooth and detailed configurations that differentiate electric and internal combustion vehicles.

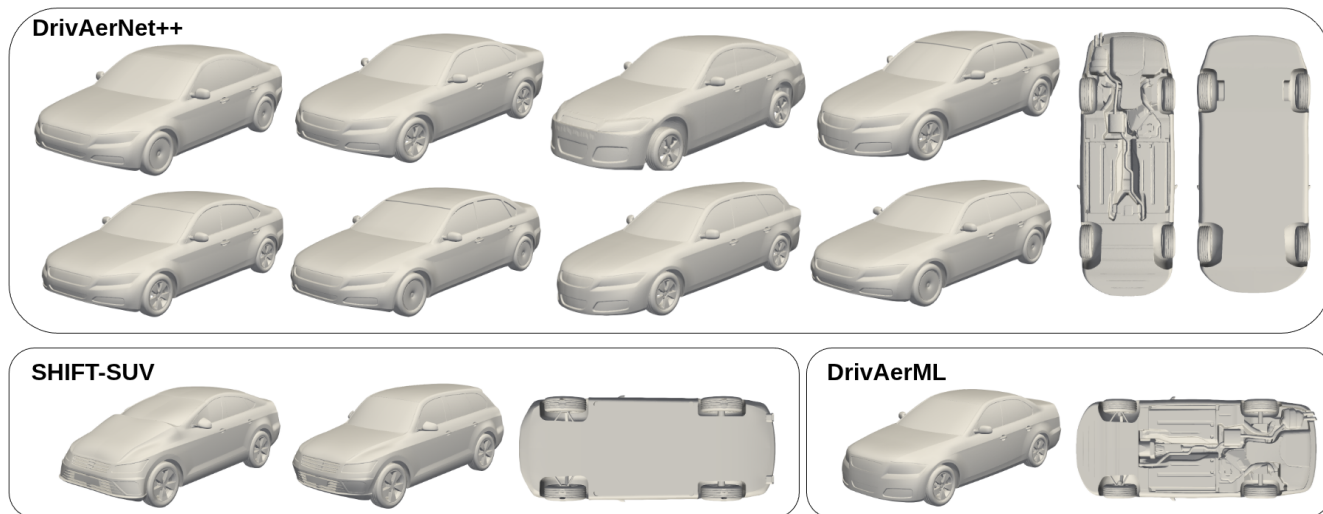


**Figure 7.** Comparison of large-scale, high-fidelity, and industry-standard open-source car datasets. DrivAerNet++ (8,150 designs, based on **eight parametric models**) provides the broadest coverage, modeling both detailed underbodies representative of internal combustion engine (ICE) cars and smooth underbodies for electric vehicles (EVs). It is also the only dataset to incorporate wheel and tire shape variations, including open and closed wheel designs. DrivAerML (~484 designs) is derived from a single DrivAer parametric model, while SHIFT-SUV (~2,000 designs) is based on two AeroSUV baseline models.

A comparison of major open-source automotive aerodynamics datasets in terms of scale, geometric diversity, and simulation fidelity is presented in Figure 7. DrivAerNet++, comprising 8,150 car designs generated from eight parametric base archetypes, exhibits the broadest geometric coverage among existing datasets. It includes both detailed underbodies representative of internal combustion vehicles and smooth configurations typical of electric vehicles, alongside diverse wheel and tire variants (open, closed, detailed, and smooth) that are critical for accurately modeling wake dynamics. All simulations were performed using steady Reynolds-Averaged Navier–Stokes (RANS) computations with the  $k-\omega$  SST turbulence model<sup>38</sup>, ensuring consistent aerodynamic fidelity across thousands of designs. In contrast, datasets such as SHIFT-SUV<sup>19</sup>, derived from only two parametric AeroSUV archetypes<sup>39</sup> and employing transient Detached Eddy Simulation (DES), and DrivAerML<sup>17</sup>, based on a single DrivAer geometry<sup>40,41</sup> simulated using Hybrid RANS–LES (HRLES), offer limited geometric and categorical diversity. DrivAerNet++ provides a complementary balance, roughly sixteen times larger than DrivAerML and four times larger than SHIFT-SUV, while maintaining standardized steady-state RANS fidelity suitable for large-scale benchmarking and model comparison. To further examine geometric variability, Figure 8 visualizes dataset distributions using Principal Component Analysis (PCA). Each point represents a distinct car geometry embedded in a reduced shape feature space, revealing clear differences in design-space coverage across datasets. DrivAerNet++ spans a broad and continuous region of the design manifold, capturing smooth morphological transitions between archetypes. By comparison, DrivAerML occupies a compact subregion almost entirely contained within the DrivAerNet++ distribution, consistent with its origin from the DrivAer Notchback baseline. SHIFT-SUV forms a distinct, narrow cluster reflecting production-grade SUV geometries with limited topological variation.

Overall, DrivAerNet++ achieves the most extensive geometric coverage among publicly available automotive CFD datasets, encompassing both continuous intra-category variations and distinct inter-category separations across Fastback, Estateback, and Notchback configurations. This diversity ensures that trained models encounter a wide spectrum of aerodynamic phenomena, from roof curvature and underbody shaping to wheel enclosure design, enabling more robust generalization to unseen geometries.

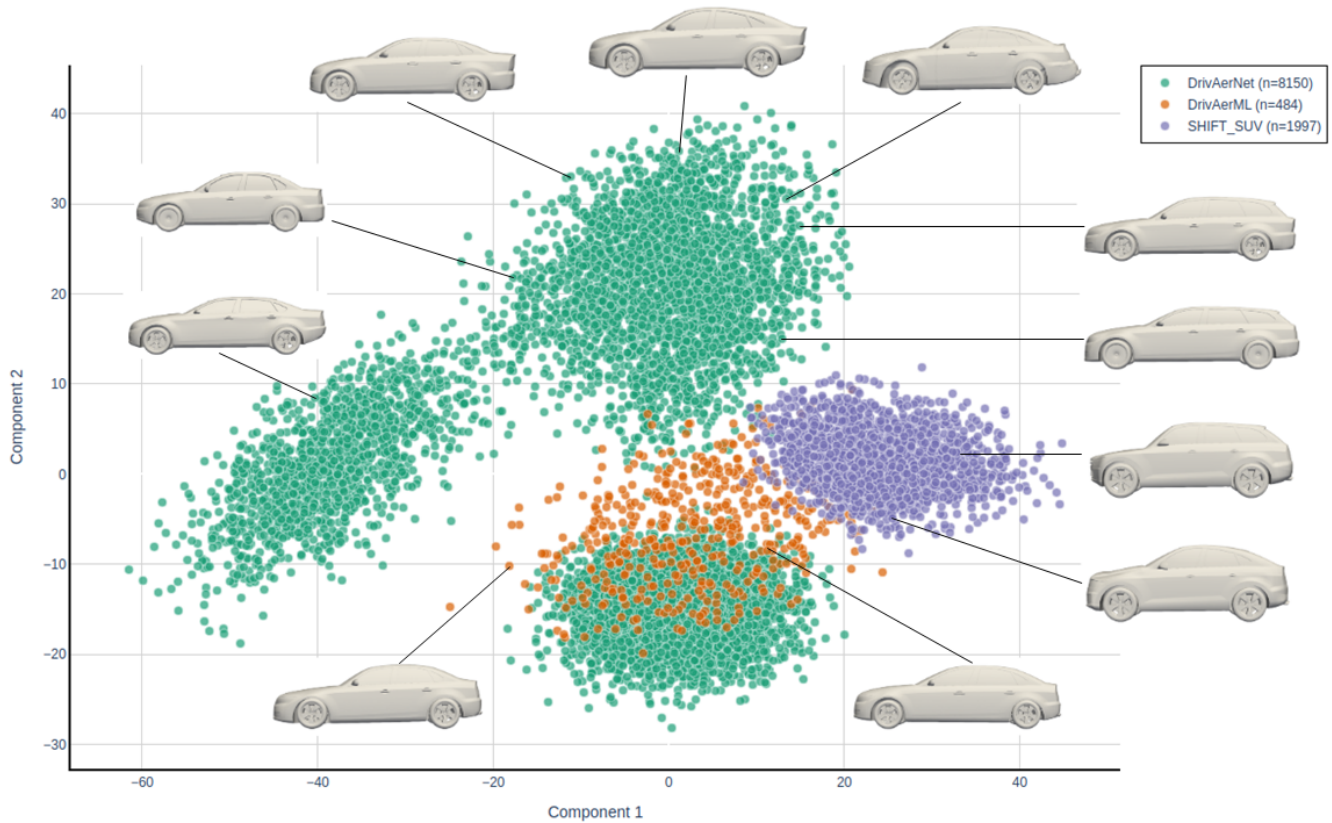


**Figure 8.** PCA projection of dataset distributions across DrivAerNet++, DrivAerML, and SHIFT-SUV. Each point represents a car geometry, with DrivAerNet++ spanning a wider and more continuous design space, while DrivAerML and SHIFT-SUV are confined to narrower regions. Notably, DrivAerML lies largely within the coverage of DrivAerNet++, as it is derived from the DrivAer Notchback baseline, one of the eight parametric archetypes used to construct DrivAerNet++. This highlights the geometric diversity and design-space coverage of DrivAerNet++.

## Data Processing and Quality Assurance

**Train/Validation/Test Splits.** For consistency and reproducibility, we adopt the official train/validation/test split provided in the DrivAerNet++ repository<sup>3</sup>. These predefined splits ensure that evaluation is performed strictly on unseen geometries, preventing any overlap between training and test samples across the full parametric design space.

**Pressure Statistics Computation.** To prevent data leakage, pressure normalization statistics are computed exclusively from the DrivAerNet++ training set containing 5,819 samples. The computation pipeline processes all VTK files corresponding to training design IDs, loading each file using PyVista<sup>42</sup> and extracting pressure field data from the computational mesh points. All pressure values from the training files are aggregated into a single array, from which population statistics are computed, including the mean  $\mu_p$  and standard deviation  $\sigma_p$ . Additional distribution characteristics, such as minimum, maximum, median, and quartiles, are also calculated. These training-only statistics provide the normalization parameters ( $\mu_p, \sigma_p$ ) used throughout the neural network pipeline. Importantly, all evaluation metrics, including relative L1 and L2 errors, are computed in the denormalized (original physical) space to ensure meaningful comparisons across different models and datasets, while maintaining strict separation between training and validation/test statistics.

Figure 9 highlights the substantial geometric complexity captured in the DrivAerNet++ surface meshes. The consistently high point and cell counts, often reaching several hundred thousand per design, reflect a high-fidelity surface discretization that preserves subtle geometric features across all vehicle classes. This level of detail creates a challenging learning setting because models must generalize across a wide spectrum of shapes with significant variability in proportions, curvature, and surface topology. This geometric diversity closely mirrors the exploration space encountered in early conceptual design stages, where broad shape variations must be evaluated efficiently. By combining high-resolution fidelity with large inter-design variability, DrivAerNet++ provides a rigorous testbed for data-driven aerodynamic prediction and design space learning.

<sup>3</sup>[https://github.com/Mohamedelrefaie/DrivAerNet/tree/main/train\\_val\\_test\\_splits](https://github.com/Mohamedelrefaie/DrivAerNet/tree/main/train_val_test_splits)

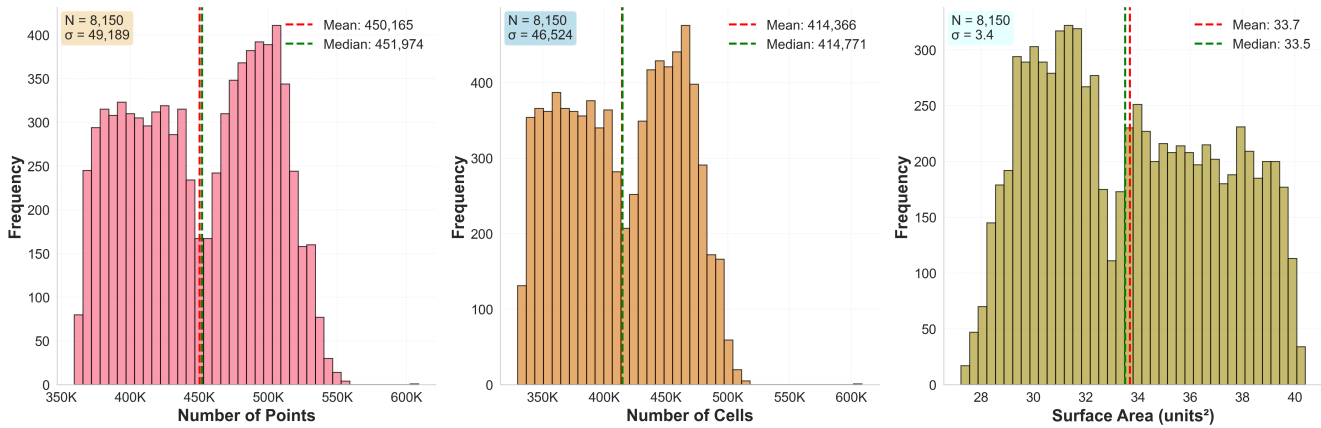


**Figure 9.** DrivAerNet++ dataset geometric statistics. Left: Distribution of point counts across all meshes, showing a consistent resolution with mean and median values around 450K. Middle: Distribution of cell counts, exhibiting a similar bimodal trend and central tendency to the point distribution. Right: Distribution of total surface area, indicating moderate variation across designs with a mean of 33.7 units<sup>2</sup>. Each subplot reports dataset size ( $N = 8,150$ ) and standard deviation, providing an overview of mesh density and geometric uniformity across the corpus.

## Automated Training and Evaluation Framework

A central goal of this work is to establish a standardized, transparent, and easily extensible framework for evaluating machine learning models in large-scale CFD predictions. Despite rapid progress in this domain, inconsistent data preprocessing, metric definitions, and training protocols have often hindered fair comparison across studies. To address this, we designed an automated benchmark pipeline that ensures full reproducibility and uniform evaluation across architectures, ranging from classical geometric deep learning models to neural operators and implicit field networks. The framework is configuration-driven, modular, and open-source, enabling both state-of-the-art replication and straightforward integration of new models. We developed an automated and model-agnostic framework to train and evaluate all machine learning baselines in a unified and reproducible manner. Each model is encapsulated within a modular wrapper that standardizes data preprocessing, normalization, and forward-pass interfaces, ensuring consistent input-output behavior across architectures. The framework is built around a *UnifiedTrainer* class that manages key aspects of training, including mixed-precision computation for efficiency, gradient clipping for stability, adaptive learning rate scheduling, and early stopping based on validation metrics. All runs automatically log losses, learning rates, and generalization gaps throughout training to facilitate transparent comparison.

For evaluation, a dedicated *UnifiedEvaluator* computes a consistent suite of quantitative metrics, including Mean Absolute Error (MAE), Root Mean Square Error (RMSE), Relative L2 error, and inference latency. These metrics are tracked across models and datasets under identical sampling conditions to ensure a fair comparison of predictive performance and computational efficiency. The framework is designed to support seamless integration of new architectures and researchers can register additional models through standardized configuration files without modifying core training scripts. This automation ensures experiment reproducibility, eliminates inconsistencies due to model-specific hyperparameters, and enables rigorous benchmarking of future models on the same evaluation protocol. Table 5 summarizes the architectural and training configurations of all machine learning baselines used in the benchmark. All models are trained under unified experimental controls, including identical point sampling strategies, consistent normalization, mixed-precision optimization, and common early stopping criteria. For the subset of baselines that we retrain within our pipeline (Table 5), this standardization substantially reduces confounding from training setup and makes performance differences easier to attribute to architectural choices. AB-UPT and TripNet are evaluated using publicly released checkpoints from the original authors, so their results should be interpreted as best-effort but not strictly normalized to the same training budget as the in-house models.

**Design Principles.** The benchmark was built around three guiding principles: (1) *standardization*: all models are trained and evaluated under identical data sampling, normalization, and metric definitions; (2) *reproducibility*: every experiment is defined via declarative configuration files with fixed random seeds and logged metadata; and (3) *accessibility*: new architectures can be integrated with minimal code overhead.

**Unified Experimental Pipeline.** Experiments are defined in YAML configuration files specifying dataset splits, sampling strategies, optimizer settings, learning rate schedulers, and early-stopping criteria. All models are evaluated using 10,000 uniformly sampled surface points per geometry, guaranteeing consistency in data input dimensionality.

**Table 5.** Training and model configurations for all ML baselines used in our benchmark. All models are trained on 10,000 points per surface sample with mean squared error loss except where noted.

Model	Training Configuration							Model Architecture					
	Loss	Epochs	LR	Opt	Batch	WD	Scheduler	Layers	Heads	Embed	Dropout	$k$ -NN	Extra
PointNet	MSE	150	$10^{-3}$	Adam	12	$10^{-4}$	ReduceLR	–	–	1024	0.3	–	–
PointNetLarge	MSE	150	$10^{-4}$	AdamW	8	$10^{-4}$	OneCycle	–	–	4096	0.3/0.5	–	Residual
RegDGCNN	MSE	200	$10^{-3}$	Adam	12	$10^{-4}$	ReduceLR	3	–	1024	0.4	40	EdgeConv
PointMAE	SmoothL1	100	$10^{-4}$	AdamW	128	$10^{-2}$	Cosine	4	–	256	0.3/0.2	–	Efficient
NeuralOperator	MSE	100	$2 \times 10^{-3}$	AdamW	16	$10^{-4}$	Cosine	2	–	16	–	–	Grid= $32^3$ , $M=8$
PointTransformer	MSE	200	$10^{-4}$	AdamW	8	$10^{-2}$	CosineWU	12	–	128	0.1	16	Local attn
Transolver	MSE	250	$10^{-3}$	Adam	64	0	StepLR	5	8	256	0.0	–	32 slices
Transolver++	MSE	200	$10^{-3}$	Adam	8	0	StepLR	5	8	256	0.0	–	32 slices, UPE
TransolverLarge	MSE	300	$10^{-4}$	Adam	1	0	StepLR	7	12	384	0.1	–	48 slices

**Notes.** (1) **WD:** Weight decay. **Opt:** Optimizer. **UPE:** Unified position encoding. (2) **Scheduler details:** ReduceLR = ReduceLRonPlateau (patience=10, factor=0.1, min\_lr= $10^{-7}$ ); OneCycle (max\_lr= $10^{-2}$ ); Cosine ( $T_{\max}$ =epochs); CosineWU = Cosine with warmup (5 epochs,  $T_0=50$ ); StepLR (step=150 for Transolver, step=50 for Transolver++, step=150 for TransolverLarge,  $\gamma=0.1$ ). (3) All models use gradient clipping (norm=1.0) and early stopping (patience: 20 for point models, 30 for transformers, 50 for TransolverLarge). (4) Mixed precision: Enabled for all except NeuralOperator (disabled for FFT stability) and TransolverLarge (disabled for training stability). (5) PointNetLarge uses dual dropout (0.3 early, 0.5 deep layers) and residual skip connections. (6) PointMAE uses an efficient encoder-decoder architecture (no transformers/attention) with SmoothL1 loss ( $\delta=1.0$ ) and dual dropout (0.3 early, 0.2 later decoder stages). (7) NeuralOperator operates on  $32^3$  voxel grids with 8 Fourier modes per dimension, 2 spectral convolution layers, width 16, GELU activation, and trilinear interpolation back to points with pointwise refinement network ( $1 \rightarrow 32 \rightarrow 16 \rightarrow 1$ ). (8) PointTransformer uses local self-attention with 16 nearest neighbors per point. (9) Transolver models use physics-aware attention with soft slices per head (32 for standard/++, 48 for Large); Transolver++ adds unified position encoding with  $8^3$  reference grid. (10) Transolver++ supports both 6D surface-only and 7D SDF modes. (11) TransolverLarge uses increased capacity: 384 hidden dim (vs 256), 7 layers (vs 5), 12 heads (vs 8), 48 slices (vs 32), MLP ratio=2 (same as standard, vs 1 for ++), achieving 7.58M parameters.

**Standardized Evaluation Metrics.** The benchmark computes a unified set of metrics for all models, covering absolute errors (MAE, MSE, RMSE), relative errors (Relative L2), and statistical measures (median relative error and P50/P90/P95/P99 percentiles of absolute error). All quantities are expressed in physically meaningful units ( $\text{m}^2/\text{s}^2$  for kinematic pressure). Model performance is further analyzed in terms of  $R_{\text{test}}^2$ , computational throughput (samples/s), memory footprint (GB), and latency (ms), under matched batch size and GPU configurations.

**Automation and Reporting.** Training, validation, and evaluation are executed via a single command-line interface, automatically generating structured logs, plots, and result tables in CSV and JSON formats.

**Extensibility and Community Contribution.** The benchmark is intentionally designed for extensibility. Researchers can contribute new architectures, loss functions, or evaluation tasks by adding configuration files and registering modules without altering the core codebase. All newly added metrics are automatically incorporated into the final evaluation pipeline. This modular design encourages collaborative benchmarking and continuous expansion of the aerodynamic learning ecosystem, fostering an open, evolving standard for machine learning in CFD.

**Preprocessed Data Release.** To facilitate accessibility and accelerate experimentation, we also release the preprocessed version of the DrivAerNet++ dataset. The data are organized in a standardized, serialized file format, containing normalized surface pressure and geometric point-cloud representations for all samples. This version significantly reduces the need for manual preprocessing or CFD file parsing, enabling researchers to directly load the dataset into training pipelines with minimal overhead. By providing ready-to-use data splits and consistent normalization statistics, the preprocessed release ensures faster training, reproducibility, and seamless integration with new models.

## Limitations and Future Work

While CarBench represents a significant step toward standardized and high-fidelity aerodynamic surrogate evaluation, several limitations must be acknowledged. The current evaluation protocol focuses primarily on pointwise error metrics such as Rel L2 and MAE, along with computational efficiency measures. Although these metrics are essential for benchmarking, they do not directly quantify discrepancies in global aerodynamic quantities. Future extensions of the benchmark will incorporate physically meaningful integrals, including lift and drag coefficients, integrated force vectors, and descriptors of flow topology, to better assess the practical relevance of surrogate predictions in design tasks.

A further limitation relates to uncertainty quantification in model training. Due to the significant computational cost associated with training eleven high-capacity neural architectures on more than five thousand samples, each model in this study was trained only once. This means that run-to-run stochastic variability, including differences caused by random initialization or optimizer noise, is not captured. In many benchmarking settings, multiple independent training runs are performed to quantify

this variance and ensure that conclusions are not influenced by unusually favorable or unfavorable single runs. We therefore report the single-run protocol as a limitation of the present study, and future benchmark iterations may incorporate multi-run analyses as computational resources allow.

Overall, we envision CarBench as a living framework that will continue to expand in scope and fidelity. Future developments may include additional physical tasks, broader flow regimes, diverse design domains, and deeper integration with design optimization and real-time simulation pipelines. We invite the community to extend, refine, and build upon this resource to advance robust, generalizable, and physically grounded machine learning for fluid dynamics.

## Community Contributions and Future Extensions

We encourage contributions from the research community to extend this benchmark with additional models and learning tasks. In particular, future releases will integrate recently proposed architectures that have demonstrated promising performance, such as *LRQ-Solver*<sup>43</sup>, *FigConvNet*<sup>33</sup>, *GAOT*<sup>44</sup>, and *AeroGTO*<sup>20</sup>, as well as expand beyond surface pressure prediction to include full volumetric flow field estimation. Through continuous collaboration and open benchmarking, we aim to establish a long-term, evolving standard for data-driven aerodynamic learning.

## Acknowledgments

We gratefully acknowledge the funding support from the Toyota Research Institute (TRI). We thank Johannes Brandstetter and Richard Kurle for sharing the pretrained AB-UPT model. We are especially grateful to Richard Kurle for his thoughtful feedback and valuable insights on benchmarking methodologies and the evaluation of machine learning models for aerodynamic prediction. We also thank Qian Chen for assisting with benchmarking the TripNet model. Finally, we thank Luminary Cloud and Michael Emory for providing access to the SHIFT-SUV dataset.

## Author Contributions Statement

M.E. conceived the study, developed the benchmark framework, implemented all experiments, performed the analyses, and prepared the manuscript. D.S. and M.K. contributed to discussions related to the project scope and provided feedback during the development of the benchmark. F.A. supervised the research, provided guidance on experimental design and interpretation, and contributed to manuscript review and refinement. All authors reviewed and approved the final version of the manuscript.

## Additional information

**Accession codes.** The DrivAerNet++ dataset is publicly available at <https://dataverse.harvard.edu/dataverse/DrivAerNet>, released under the Creative Commons Attribution–NonCommercial 4.0 International License (CC BY–NC 4.0). All benchmarking code, evaluation scripts, and pretrained model weights used in this study will be released publicly upon paper acceptance to ensure full reproducibility and transparent comparison.

**Competing interests.** The authors declare no competing financial or non-financial interests.

**Correspondence.** Correspondence should be addressed to Mohamed Elrefaie ([mohamed.elrefaie@mit.edu](mailto:mohamed.elrefaie@mit.edu)).

## References

1. Deng, J. *et al.* Imagenet: A large-scale hierarchical image database. In *2009 IEEE conference on computer vision and pattern recognition*, 248–255 (Ieee, 2009).
2. Krizhevsky, A., Sutskever, I. & Hinton, G. E. Imagenet classification with deep convolutional neural networks. *Adv. neural information processing systems* **25** (2012).
3. Wang, A. *et al.* Glue: A multi-task benchmark and analysis platform for natural language understanding. *arXiv preprint arXiv:1804.07461* (2018).
4. Wang, A. *et al.* Superglue: A stickier benchmark for general-purpose language understanding systems. *Adv. neural information processing systems* **32** (2019).
5. Hendrycks, D. *et al.* Measuring massive multitask language understanding. *arXiv preprint arXiv:2009.03300* (2020).
6. Devlin, J., Chang, M.-W., Lee, K. & Toutanova, K. Bert: Pre-training of deep bidirectional transformers for language understanding. In *Proceedings of the 2019 conference of the North American chapter of the association for computational linguistics: human language technologies, volume 1 (long and short papers)*, 4171–4186 (2019).
7. Brown, T. *et al.* Language models are few-shot learners. *Adv. neural information processing systems* **33**, 1877–1901 (2020).

8. Elrefaie, M. *et al.* Surrogate modeling of the aerodynamic performance for airfoils in transonic regime. In *AIAA SCITECH 2024 Forum*, 2220 (2024).
9. Sung, N. *et al.* Blendednet: A blended wing body aircraft dataset and surrogate model for aerodynamic predictions. *arXiv preprint arXiv:2509.07209* (2025).
10. Elrefaie, M., Dai, A. & Ahmed, F. Drivaernet: A parametric car dataset for data-driven aerodynamic design and graph-based drag prediction. In *International Design Engineering Technical Conferences and Computers and Information in Engineering Conference*, vol. 88360, V03AT03A019 (American Society of Mechanical Engineers, 2024).
11. Elrefaie, M., Morar, F., Dai, A. & Ahmed, F. Drivaernet++: A large-scale multimodal car dataset with computational fluid dynamics simulations and deep learning benchmarks. *Adv. Neural Inf. Process. Syst.* **37**, 499–536 (2024).
12. Wu, H., Luo, H., Wang, H., Wang, J. & Long, M. Transolver: A fast transformer solver for pdes on general geometries. *arXiv preprint arXiv:2402.02366* (2024).
13. Luo, H. *et al.* Transolver++: An accurate neural solver for pdes on million-scale geometries. *arXiv preprint arXiv:2502.02414* (2025).
14. Alkin, B. *et al.* Ab-upt: Scaling neural cfd surrogates for high-fidelity automotive aerodynamics simulations via anchored-branched universal physics transformers. *arXiv preprint arXiv:2502.09692* (2025).
15. Jacob, S. J., Mrosek, M., Othmer, C. & Köstler, H. Deep learning for real-time aerodynamic evaluations of arbitrary vehicle shapes. *arXiv preprint arXiv:2108.05798* (2021).
16. Jacob, S. J., Mrosek, M., Othmer, C. & Köstler, H. Benchmarking convolutional neural network and graph neural network based surrogate models on a real-world car external aerodynamics dataset. *arXiv preprint arXiv:2504.06699* (2025).
17. Ashton, N. *et al.* Drivaerml: High-fidelity computational fluid dynamics dataset for road-car external aerodynamics. *arXiv preprint arXiv:2408.11969* (2024).
18. Ashton, N., Maddix, D. C., Gundry, S. & Shabestari, P. M. Ahmedml: High-fidelity computational fluid dynamics dataset for incompressible, low-speed bluff body aerodynamics. *arXiv preprint arXiv:2407.20801* (2024).
19. Luminary-Cloud. Shift-suv: High-fidelity computational fluid dynamics dataset for suv external aerodynamics. <https://huggingface.co/datasets/luminary-shift/SUV> (2025). Accessed: 2025-10-19.
20. Liu, P. *et al.* Aerocto: An efficient graph-transformer operator for learning large-scale aerodynamics of 3d vehicle geometries. In *Proceedings of the AAAI Conference on Artificial Intelligence*, vol. 39, 18924–18932 (2025).
21. Tangsali, K. *et al.* A benchmarking framework for ai models in automotive aerodynamics. *arXiv preprint arXiv:2507.10747* (2025).
22. Schuetz, T. C. *Aerodynamics of road vehicles* (Sae International, 2015).
23. Sudin, M. N., Abdullah, M. A., Shamsuddin, S. A., Ramli, F. R. & Tahir, M. M. Review of research on vehicles aerodynamic drag reduction methods. *Int. J. Mech. Mechatronics Eng.* **14**, 35–47 (2014).
24. Li, Z. *et al.* Fourier neural operator for parametric partial differential equations. *arXiv preprint arXiv:2010.08895* (2020).
25. Qi, C. R., Su, H., Mo, K. & Guibas, L. J. Pointnet: Deep learning on point sets for 3d classification and segmentation. In *Proceedings of the IEEE conference on computer vision and pattern recognition*, 652–660 (2017).
26. Elrefaie, M., Dai, A. & Ahmed, F. Drivaernet: A parametric car dataset for data-driven aerodynamic design and prediction. *J. Mech. Des.* **147**, 041712 (2025).
27. Zhao, H., Jiang, L., Jia, J., Torr, P. H. & Koltun, V. Point transformer. In *Proceedings of the IEEE/CVF international conference on computer vision*, 16259–16268 (2021).
28. Pang, Y., Tay, E. H. F., Yuan, L. & Chen, Z. Masked autoencoders for 3d point cloud self-supervised learning. *World Sci. Annu. Rev. Artif. Intell.* **1**, 2440001 (2023).
29. Chen, Q., Elrefaie, M., Dai, A. & Ahmed, F. Tripnet: Learning large-scale high-fidelity 3d car aerodynamics with triplane networks. *arXiv preprint arXiv:2503.17400* (2025).
30. Brandt, A., Berg, H., Bolzon, M. & Josefsson, L. The effects of wheel design on the aerodynamic drag of passenger vehicles. *SAE Int. J. Adv. Curr. Pract. Mobil.* **1**, 1279–1299 (2019).
31. Pfadenhauer, M., Wickern, G. & Zwicker, K. On the influence of wheels and tyres on the aerodynamic drag of vehicles. In *MIRA international conference on vehicle aerodynamics* (1996).

32. Hucho, W.-H. *Aerodynamik des Automobils: eine Brücke von der Strömungsmechanik zur Fahrzeugtechnik* (Springer-Verlag, 2013).
33. Choy, C. *et al.* Factorized implicit global convolution for automotive computational fluid dynamics prediction. *arXiv preprint arXiv:2502.04317* (2025).
34. Efron, B. Bootstrap methods: another look at the jackknife. In *Breakthroughs in statistics: Methodology and distribution*, 569–593 (Springer, 1992).
35. Efron, B. & Tibshirani, R. J. *An introduction to the bootstrap* (Chapman and Hall/CRC, 1994).
36. Vatani, P., Elrefaie, M., Nazarpour, F. & Ahmed, F. Triptimizer: Generative 3d shape optimization and drag prediction using triplane vae networks. *arXiv preprint arXiv:2509.12224* (2025).
37. Elrefaie, M. *et al.* Ai agents in engineering design: a multi-agent framework for aesthetic and aerodynamic car design. *arXiv preprint arXiv:2503.23315* (2025).
38. Menter, F. R., Kuntz, M., Langtry, R. *et al.* Ten years of industrial experience with the sst turbulence model. *Turbul. heat mass transfer* **4**, 625–632 (2003).
39. European Car Aerodynamic Research Association (ECARA). Aerosuv / drivaer reference models — data exchange. <https://www.ecara.org/drivaer-1> (2019). Accessed: 2025-10-20.
40. Heft, A. I., Indinger, T. & Adams, N. A. Introduction of a new realistic generic car model for aerodynamic investigations. Tech. Rep., SAE Technical Paper (2012).
41. Chair of Aerodynamics and Fluid Mechanics, Technical University of Munich. Drivaer model geometry. <https://www.epc.ed.tum.de/en/aer/research-groups/automotive/drivaer/geometry/>. Accessed: 2025-10-20.
42. Sullivan, B. & Kaszynski, A. PyVista: 3D plotting and mesh analysis through a streamlined interface for the Visualization Toolkit (VTK). *J. Open Source Softw.* **4**, 1450, DOI: [10.21105/joss.01450](https://doi.org/10.21105/joss.01450) (2019).
43. Zeng, P. *et al.* Lrq-solver: A transformer-based neural operator for fast and accurate solving of large-scale 3d pdes. *arXiv preprint arXiv:2510.11636* (2025).
44. Wen, S. *et al.* Geometry aware operator transformer as an efficient and accurate neural surrogate for pdes on arbitrary domains. *arXiv preprint arXiv:2505.18781* (2025).
45. Takamoto, M. *et al.* Pdebench: An extensive benchmark for scientific machine learning. *Adv. Neural Inf. Process. Syst.* **35**, 1596–1611 (2022).
46. Yagoubi, M. *et al.* Neurips 2024 ml4cfd competition: Harnessing machine learning for computational fluid dynamics in airfoil design. *arXiv preprint arXiv:2407.01641* (2024).
47. Rabeh, A. *et al.* Benchmarking scientific machine-learning approaches for flow prediction around complex geometries. *Commun. Eng.* **4**, 182 (2025).
48. Bekemeyer, P., Hariharan, N., Wissink, A. M. & Cornelius, J. Introduction of applied aerodynamics surrogate modeling benchmark cases. In *AIAA SCITECH 2025 Forum*, 0036 (2025).
49. Li, Z. *et al.* Geometry-informed neural operator for large-scale 3d pdes. *Adv. Neural Inf. Process. Syst.* **36**, 35836–35854 (2023).
50. Umetani, N. & Bickel, B. Learning three-dimensional flow for interactive aerodynamic design. *ACM Transactions on Graph. (TOG)* **37**, 1–10 (2018).
51. Greenshields, C. Openfoam v11 user guide. the openfoam foundation, london (2023).
52. Wang, Y. *et al.* Dynamic graph cnn for learning on point clouds. *ACM Transactions on Graph. (tog)* **38**, 1–12 (2019).
53. Lighthill, M. J. On sound generated aerodynamically i. general theory. *Proc. Royal Soc. London. Ser. A. Math. Phys. Sci.* **211**, 564–587 (1952).
54. Oettle, N. & Sims-Williams, D. Automotive aeroacoustics: An overview. *Proc. Inst. Mech. Eng. Part D: J. Automob. Eng.* **231**, 1177–1189 (2017).

## Appendix

### Existing Benchmarks Comparison

Recent initiatives have introduced standardized benchmarks for learning-based scientific simulation, providing unified datasets, evaluation metrics, and experimental pipelines across various physics domains. PDEBench<sup>45</sup> offers a broad suite of time-dependent PDE problems, including advection, Burgers’, compressible Navier–Stokes, and Darcy flow, together with baseline neural solvers to support reproducible scientific machine learning. The NeurIPS 2024 ML4CFD Competition<sup>46</sup> advanced benchmarking in external aerodynamics by evaluating surrogate models on the AirfRANS dataset via a multi-criteria framework that emphasizes not only predictive accuracy but also inference efficiency and out-of-distribution robustness. Complementing these efforts, Rabeh et al.<sup>47</sup> systematically compared scientific machine-learning architectures for steady-state flow prediction around complex shapes, assessing global error, boundary-layer fidelity, and physical consistency through a unified scoring protocol. Bekemeyer et al.<sup>48</sup> expanded benchmarking for applied aerodynamics by introducing four well-documented test cases for surrogate modeling of airfoils, missiles, and three-dimensional aerodynamic surfaces. Their work highlights the need for standardized formats, rigorous documentation, and reproducible pipelines in surrogate-based aerodynamic modeling.

**Table 6.** Comparison of existing CFD-based automotive aerodynamics datasets and benchmarks. Each entry lists the corresponding study and dataset, characterized by simulation scale, test set size, number of design categories, number of evaluated machine learning models, flow regime, and benchmark availability. DrivAerNet++ is the largest and most diverse open dataset, supporting full-field aerodynamic supervision, standardized benchmarking, and cross-category generalization across distinct car archetypes. RANS stands for Reynolds-Averaged Navier–Stokes Simulation, DES stands for Detached Eddy Simulation, and LES for Large Eddy Simulation. Bold values indicate the best entries, while underlined values indicate the second best. \*Note that the VW Real-World benchmark evaluates only drag coefficients and does not provide full-field flow supervision.

Study	Dataset	Simulations	Test Size	Design Categories	# Models Evaluated	Flow Regime	Benchmark Availability	Cross-Category Generalization	Uncertainty Quantification
CarBench (Ours)	DrivAerNet++	<b>8,150</b>	<b>1,154</b>	<u>8</u>	<u>11</u>	Steady RANS (OpenFOAM)	✓	✓	✓
Jacob et al. <sup>16</sup>	VW Real-World*	343	69	<b>32</b>	2	DES (OpenFOAM)	✗	✗	✗
Li et al. <sup>49</sup>	ShapeNet-Car	889	100	1	5	Steady RANS (OpenFOAM)	✗	✗	✗
Tangsali et al. <sup>21</sup>	DrivAerML	484	48	1	3	Hybrid RANS-LES (OpenFOAM)	✓	✗	✗
Li et al. <sup>49</sup>	Ahmed body	551	51	1	5	Steady RANS (OpenFOAM)	✗	✗	✗
Luo et al. <sup>13</sup>	DrivAerNet++	200	10	3	<b>13</b>	Steady RANS (OpenFOAM)	✗	✗	✗
Jacob et al. <sup>15</sup>	VW Internal	<u>1000</u>	<u>150</u>	2	3	Lattice Boltzmann (ultraFluidX)	✗	✗	✗

While these initiatives represent important progress, they primarily focus on lower-dimensional PDE settings or simplified aerodynamic configurations. Only a limited number of datasets address high-resolution three-dimensional shapes, and fewer still offer sufficient diversity to support meaningful generalization studies. To contextualize this landscape, Table 6 compares existing 3D CFD-based datasets for automotive aerodynamics in terms of scale, category diversity, availability of full-field flow data, and benchmark completeness.

Despite their contributions, current benchmarks leave several open gaps. Transolver++ by Luo et al.<sup>13</sup> provides one of the earliest attempts at benchmarking transformer-based PDE solvers across multiple CFD tasks, but its evaluation on DrivAerNet++ relies on only 200 simulations and ten test samples across three car categories. Although useful for proof-of-concept validation, such limited sampling cannot capture the geometric and aerodynamic diversity needed to assess model robustness or cross-category transfer. Similarly, the Volkswagen Real-World dataset<sup>16</sup> represents a valuable step toward connecting academic and industrial CFD workflows, containing 343 simulations across 32 production car designs. However, its exclusive focus on drag coefficient prediction, coupled with the absence of full-field aerodynamic supervision, constrains its suitability for training general-purpose surrogate models. Moreover, the VW Real-World<sup>16</sup> and VW Internal<sup>15</sup> datasets represent valuable contributions from industry that help bridge academic and real-world CFD workflows. However, both datasets are proprietary, which limits reproducibility and broader accessibility for the open research community. Other open datasets, such as ShapeNet-Car<sup>50</sup> and the Ahmed body geometries<sup>49</sup> provide 889 and 551 RANS simulations, respectively, but contain only a single vehicle class, making them insufficient for cross-category generalization or broad aerodynamic design tasks. More recently, the PhysicsNeMo benchmark<sup>21</sup> introduced an evaluation framework based on the open-source PhysicsNeMo-CFD toolkit. However, its scale remains modest (484 simulations with 48 test cases), and its benchmark lacks uncertainty quantification, category diversity, and the breadth of aerodynamic supervision required for benchmarking modern deep learning models.

In contrast, **CarBench** introduces the first open, large-scale, and geometrically diverse benchmark dedicated specifically to high-resolution three-dimensional external aerodynamics. Built on 8,150 steady-state RANS simulations across eight parametric car archetypes from DrivAerNet++, CarBench supports full-field aerodynamic supervision, standardized train–validation–test

splits (including 1,154 held-out test samples), model-agnostic evaluation metrics, and rigorous uncertainty quantification. Its consistent numerical settings, balanced archetype representation, and explicit support for cross-category generalization together provide the scale and diversity required to evaluate modern geometric deep learning, neural operator, and transformer-based solvers. By combining statistical representativeness, reproducible pipelines, and a comprehensive suite of aerodynamic tasks, CarBench fills a critical gap in the landscape of physics-based ML benchmarking and enables fair, rigorous, and large-scale comparison of learning-based aerodynamic models for the first time.

## Evaluation Metrics

To rigorously evaluate the performance of the models, we employ a set of well-established metrics that quantify the accuracy, error, and generalization capabilities of the predictions. These metrics are defined as follows:

- **Mean Absolute Error (MAE):** The MAE measures the average magnitude of absolute errors between the predicted values ( $\hat{y}_i$ ) and the ground truth values ( $y_i$ ). It is defined as:

$$\text{MAE} = \frac{1}{N} \sum_{i=1}^N |\hat{y}_i - y_i|$$

where  $N$  is the total number of data points. This metric provides an intuitive measure of the average error magnitude, making it easy to interpret. Lower MAE values indicate better model performance.

- **Mean Squared Error (MSE):** The MSE quantifies the average of the squared differences between predicted and true values. It is expressed as:

$$\text{MSE} = \frac{1}{N} \sum_{i=1}^N (\hat{y}_i - y_i)^2$$

This metric penalizes larger deviations more severely, emphasizing outliers and high-error regions. It serves as the most common loss function during training for regression-based models and provides a direct measure of model accuracy in squared physical units (e.g.,  $\text{m}^4/\text{s}^4$  for kinematic pressure).

- **Root Mean Square Error (RMSE):** The RMSE computes the square root of the mean squared differences between predictions and ground truth. It is given by:

$$\text{RMSE} = \sqrt{\frac{1}{N} \sum_{i=1}^N (\hat{y}_i - y_i)^2}$$

RMSE penalizes larger errors more heavily than MAE due to the squaring operation, making it particularly sensitive to outliers. It is commonly used when large deviations are of greater concern.

- **Coefficient of Determination ( $R^2$ ):** The  $R^2$  metric, also known as the coefficient of determination, quantifies the proportion of variance in the ground truth that is explained by the model's predictions. It is defined as:

$$R^2 = 1 - \frac{\sum_{i=1}^N (y_i - \hat{y}_i)^2}{\sum_{i=1}^N (y_i - \bar{y})^2}$$

where  $\bar{y}$  is the mean of the ground truth values. An  $R^2$  value close to 1 indicates that the model explains most of the variance, while a value close to 0 suggests poor predictive performance.

- **Relative L2 Error:** The Relative L2 error evaluates the normalized L2 error between predictions and ground truth. It is defined as:

$$\text{Relative L2} = \frac{\|\hat{y} - y\|_2}{\|y\|_2}$$

where  $\|\cdot\|_2$  denotes the Euclidean norm. This metric provides a scale-invariant measure of error, making it particularly useful for comparing models across datasets with different scales.

- **Relative L1 Error:** The Relative L1 error computes the normalized L1 error, which is the sum of absolute differences between predictions and ground truth, normalized by the sum of absolute ground truth values:

$$\text{Relative L1} = \frac{\sum_{i=1}^N |\hat{y}_i - y_i|}{\sum_{i=1}^N |y_i|}$$

This metric is also scale-invariant and provides an alternative to Relative L2 for datasets where absolute differences are more meaningful.

- **Maximum Error:** The Maximum Error captures the largest absolute error in the predictions:

$$\text{Max Error} = \max_i |\hat{y}_i - y_i|$$

This metric highlights the worst-case performance of the model, which is critical in applications where large errors can have significant consequences.

These metrics collectively provide a comprehensive evaluation framework, capturing both absolute and relative errors, as well as the model's ability to explain variance in the data. By combining these metrics, we ensure a robust assessment of the model's predictive performance across different aspects of the problem

### **Pressure Units**

In this work, all simulations were performed using the SIMPLEFOAM solver in OPENFOAM<sup>51</sup>, which operates with *kinematic pressure* ( $p/\rho$ ) rather than absolute pressure. Kinematic pressure has SI dimensions of  $\text{m}^2 \text{s}^{-2}$ , as opposed to absolute pressure with units of  $\text{Pa} = \text{kg m}^{-1} \text{s}^{-2}$ . This formulation simplifies the pressure–velocity coupling by removing the explicit dependence on density, making it particularly suitable for incompressible steady-state flows. Consequently, all reported pressure values and visualizations in this paper are expressed in terms of the kinematic pressure. For physical interpretation or validation, these quantities can be converted to Pascals by multiplying by the reference fluid density, ensuring consistent comparison across different flow conditions. All machine learning models were trained using normalized pressure values to ensure numerical stability and balanced gradient magnitudes during optimization. During evaluation, however, results are reported in kinematic pressure units ( $\text{m}^2/\text{s}^2$ ) following the conventions of OPENFOAM. This approach combines the advantages of normalized learning, including stable convergence and scale consistency, with physically interpretable outputs at inference time. Reporting evaluation metrics such as MAE, MSE, and RMSE in physical units provides a meaningful link between model performance and aerodynamic quantities, enabling direct comparison with CFD reference data and quantifying predictive deviations in real-world terms.

## Bootstrap Confidence Intervals for Performance Metrics

To quantify the statistical reliability and uncertainty of model performance, we employed the bootstrap resampling method<sup>34</sup>. This nonparametric approach estimates the sampling distribution of a statistic by repeatedly resampling with replacement from the observed test data. Unlike parametric methods that assume Gaussian or other specific error distributions, bootstrap resampling does not rely on such assumptions, making it particularly suitable for evaluating complex performance metrics such as  $R^2$  or relative L2 error.

### Bootstrap Methodology

Given a test set  $\mathcal{D}_{\text{test}} = \{(\mathbf{x}_i, y_i)\}_{i=1}^N$ , where  $\mathbf{x}_i$  denotes the input geometry and  $y_i$  the ground-truth pressure field, we generate  $B$  bootstrap replicates  $\{\mathcal{D}_{\text{test}}^{(b)}\}_{b=1}^B$  by randomly sampling  $N$  pairs with replacement. For each replicate  $\mathcal{D}_{\text{test}}^{(b)}$ , we compute the performance metric  $\theta^{(b)} = f(\mathcal{D}_{\text{test}}^{(b)})$  (e.g., MSE,  $R^2$ , or MAE).

The bootstrap estimates of the mean and standard deviation are given by:

$$\bar{\theta}_{\text{boot}} = \frac{1}{B} \sum_{b=1}^B \theta^{(b)}, \quad \sigma_{\text{boot}} = \sqrt{\frac{1}{B-1} \sum_{b=1}^B (\theta^{(b)} - \bar{\theta}_{\text{boot}})^2}. \quad (1)$$

Confidence intervals are obtained using the *percentile method*:

$$\text{CI}_{1-\alpha} = [\theta_{\alpha/2}^*, \theta_{1-\alpha/2}^*], \quad (2)$$

where  $\theta_p^*$  denotes the  $p$ -th percentile of the bootstrap distribution.

### Implementation Details

We used the following settings in our experiments:

- **Number of bootstrap iterations:**  $B = 2000$ , ensuring stable confidence interval estimates while remaining computationally tractable<sup>35</sup>.
- **Confidence level:** 95% ( $\alpha = 0.05$ ), corresponding to the 2.5th and 97.5th percentiles.
- **Metrics evaluated:**  $R^2$ , MSE, MAE, RMSE, relative L2 error, and maximum error.

The complete algorithmic procedure is summarized in Algorithm 1.

---

#### Algorithm 1 Bootstrap Confidence Interval Estimation

---

**Require:** Test set  $\mathcal{D}_{\text{test}}$ , predictions  $\{\hat{y}_i\}_{i=1}^N$ , number of iterations  $B$

**Ensure:** Mean  $\bar{\theta}$ , confidence interval  $[\theta_{\text{lower}}, \theta_{\text{upper}}]$

- 1: Initialize list  $\Theta = []$
  - 2: **for**  $b = 1$  to  $B$  **do**
  - 3:     Sample  $N$  indices with replacement:  $\mathcal{I}^{(b)} \sim \{1, \dots, N\}$
  - 4:     Compute metric on resampled pairs:  $\theta^{(b)} = f(\{(y_i, \hat{y}_i) : i \in \mathcal{I}^{(b)}\})$
  - 5:     Append  $\theta^{(b)}$  to  $\Theta$
  - 6: **end for**
  - 7: Sort  $\Theta$  in ascending order
  - 8: Compute mean:  $\bar{\theta} = \frac{1}{B} \sum_{b=1}^B \theta^{(b)}$
  - 9: Extract 95% CI:  $\theta_{\text{lower}} = \Theta[0.025B]$ ,  $\theta_{\text{upper}} = \Theta[0.975B]$
  - 10: **return**  $\bar{\theta}$ ,  $[\theta_{\text{lower}}, \theta_{\text{upper}}]$
- 

### Interpretation and Relevance

Bootstrap confidence intervals provide several important advantages for model evaluation:

1. **Uncertainty quantification:** They provide an empirical measure of variability in model performance, distinguishing genuine improvements from random fluctuations due to finite test samples.
2. **Distribution-free robustness:** The method does not rely on normality or homoscedasticity assumptions, ensuring reliability for skewed or heavy-tailed metric distributions.

3. **Statistical comparability:** Overlapping confidence intervals between models indicate that apparent performance gaps may not be statistically significant.
4. **Stability assessment:** Narrow intervals indicate consistent generalization, while wider intervals suggest sensitivity to test-set composition.

For example, if Model A yields  $R^2 = 0.950 \pm 0.003$  (95% CI: [0.944, 0.956]) and Model B achieves  $R^2 = 0.945 \pm 0.008$  (95% CI: [0.930, 0.960]), the overlapping ranges imply no statistically significant difference despite differing point estimates. All bootstrap distributions, sample statistics, and confidence bounds were stored to facilitate reproducibility and downstream statistical analyses. This rigorous uncertainty quantification ensures that all model comparisons are statistically grounded and scientifically sound.

## Baseline Models

The following baseline models span a diverse set of architectural families widely used in geometric deep learning, including point-based, graph-based, and attention-based paradigms. Each model is adapted for dense surface-pressure regression on 3D car geometries and trained using a standardized protocol for fair comparison. Below, we describe the design choices, training setups, and architectural adaptations used for each method.

### *RegDGCNN*

The RegDGCNN model, introduced by Elrefaie et al.<sup>26</sup>, is a modified version of Dynamic Graph Convolutional Neural Networks (DGCNN)<sup>52</sup>. It constructs dynamic  $k$ -nearest neighbors graphs ( $k = 40$ ) and first applies a learnable spatial transformation network that predicts a  $3 \times 3$  alignment matrix to normalize input coordinates. Three edge convolution stages then compute edge features  $[\mathbf{x}_j - \mathbf{x}_i, \mathbf{x}_i]$ ; each stage processes these with pointwise ( $1 \times 1$ ) convolutions, Batch Normalization, and a Leaky Rectified Linear Unit (negative slope 0.2), followed by max aggregation over neighbors, yielding three local feature maps with 64 feature channels each. The concatenated local representation is projected to a global embedding of dimension 1024 and globally max-pooled across points; this global vector is broadcast back to all points, concatenated with the three local maps (for a total of 1,216 feature channels), and processed by pointwise convolutions  $256 \rightarrow 256 \rightarrow 128 \rightarrow 1$  with dropout probability 0.4 to regress one pressure value per point. Training uses 10,000 points per surface, batch size 12, and 200 epochs, with the adaptive moment estimation optimizer (learning rate  $10^{-3}$ , weight decay  $10^{-4}$ ), a reduce-on-plateau learning rate scheduler (patience 10, reduction factor 0.1, minimum learning rate  $10^{-7}$ ), mean squared error loss, automatic mixed precision, and gradient clipping with norm 1.0.

### *PointNet*

PointNet<sup>25</sup> operates on raw point coordinates  $\mathbf{X} \in \mathbb{R}^{3 \times N}$ . A learnable spatial transformation network predicts a  $3 \times 3$  alignment matrix to normalize inputs. The feature extractor applies shared pointwise convolutions with Batch Normalization and ReLU activations, mapping  $3 \rightarrow 64 \rightarrow 128 \rightarrow 1024$ , followed by global max pooling to obtain a 1024-dimensional global descriptor. For per-point regression, this global descriptor is broadcast to all points and concatenated with the intermediate 64-dimensional point features to form a 1088-dimensional per-point representation, which is processed by a shared regression head  $1088 \rightarrow 512 \rightarrow 256 \rightarrow 128 \rightarrow 1$  with Batch Normalization, Rectified Linear Unit activations, and dropout probability 0.3, yielding one pressure value per point. We modified the original PointNet architecture<sup>25</sup> to accommodate the high-dimensional per-point regression task, replacing the classification layers with a fully convolutional regression head optimized for continuous field prediction. Training uses 10,000 points per surface, batch size 12, and 150 epochs, with the adaptive moment estimation optimizer (learning rate  $10^{-3}$ , weight decay  $10^{-4}$ ), a reduce-on-plateau learning rate scheduler (patience 10, reduction factor 0.1, minimum learning rate  $10^{-7}$ ), mean squared error loss, and gradient clipping with norm 1.0.

### *PointNetLarge*

In this work, we test a larger variant of PointNet<sup>25</sup> to evaluate the effect of increased model capacity on predictive performance. The large PointNet variant operates on raw point coordinates  $\mathbf{X} \in \mathbb{R}^{3 \times N}$  and begins with a learnable spatial transformation network that predicts a  $3 \times 3$  alignment matrix to normalize input geometry. The feature extractor applies shared pointwise one-dimensional convolutions across points with channel widths  $64 \rightarrow 128 \rightarrow 256 \rightarrow 512 \rightarrow 1024 \rightarrow 2048$ , followed by a global  $1 \times 1$  convolution to 4096 dimensions and global max pooling to form a global descriptor. For per-point regression, the global descriptor is broadcast to all points and concatenated with multi-scale local features from the intermediate layers; this concatenated representation is processed by a deep per-point regression head with successive pointwise convolutions  $2048 \rightarrow 1024 \rightarrow 512 \rightarrow 256 \rightarrow 128 \rightarrow 64$ , Batch Normalization, and Rectified Linear Unit activations. Two residual connections are used via  $1 \times 1$  skip projections (from 1024 to 512 and from 256 to 128) to improve information flow, followed by final pointwise layers  $32 \rightarrow 16 \rightarrow 1$  to predict one pressure value per point. Regularization includes dropout with probability 0.3 in early stages and a heavier dropout with probability 0.5 in deeper layers. Training uses 10,000 points per surface, batch size 8, and 150 epochs with the adaptive moment estimation optimizer with decoupled weight decay (base learning rate  $10^{-4}$ , weight decay  $10^{-4}$ ), a One-Cycle learning rate policy peaking at  $10^{-2}$ , mean squared error loss, gradient clipping with norm 1.0, automatic mixed precision, and early stopping.

### *PointMAE*

We adapted an efficient encoder-decoder architecture for surface pressure field prediction, inspired by the PointMAE framework<sup>28</sup>. The model processes  $N$  input points with three-dimensional coordinates. The encoder applies shared one-dimensional convolutions with Batch Normalization and Rectified Linear Unit activations to map  $3 \rightarrow 64 \rightarrow 128 \rightarrow 256 \rightarrow 512$ , followed by a global projection  $512 \rightarrow 1024$  and global max pooling across points to obtain a scene-level descriptor. This global descriptor is broadcast back to all points and concatenated with the local encoder features (512-dimensional) and the raw coordinates (3-dimensional), forming a  $1024+512+3$ -dimensional per-point representation that is decoded by pointwise convolutions  $1539 \rightarrow 512 \rightarrow 256 \rightarrow 128 \rightarrow 64 \rightarrow 1$  with Batch Normalization, Rectified Linear Unit activations, and dropout probabilities 0.3

and 0.2 in the early decoder stages, yielding one pressure value per point. Training uses 10,000 points per surface, batch size 128, and 500 epochs with the adaptive moment estimation optimizer with decoupled weight decay (learning rate  $10^{-4}$ , weight decay  $10^{-2}$ ), a cosine learning-rate schedule (minimum learning rate  $10^{-5}$ ), the smooth L1 loss with Huber parameter 1.0, gradient clipping with norm 1.0, early stopping with patience 20 epochs, and validation every 5 epochs.

### **NeuralOperator**

The NeuralOperator model maps the input point cloud to a voxel grid of resolution  $32^3$ , using an occupancy scalar field and augmenting it with normalized grid coordinates; these four channels form the input to a three-dimensional Fourier Neural Operator<sup>24</sup>. The operator lifts inputs to a width of 16 through a linear layer, applies two spectral convolution blocks that learn complex Fourier coefficients up to 8 modes along each spatial dimension, and combines them with parallel  $1 \times 1 \times 1$  convolutions via residual connections; a Gaussian Error Linear Unit activation follows the first residual, and a final linear projection produces a single pressure channel on the grid. The grid prediction is interpolated back to the original points by trilinear sampling, then refined with a point-wise network (one-dimensional convolutions  $1 \rightarrow 32 \rightarrow 16 \rightarrow 1$  with Batch Normalization and Rectified Linear Unit activations) to yield per-point pressure. Training uses 10,000 points per surface, batch size 16, and 100 epochs with the adaptive moment estimation optimizer with decoupled weight decay (learning rate  $2 \times 10^{-3}$ , weight decay  $10^{-4}$ ), cosine learning-rate schedule with period 100 epochs, mean squared error loss, gradient clipping with norm 1.0, and mixed precision disabled due to fast Fourier transforms.

### **PointTransformer**

We employ a modified version of the PointTransformer<sup>27</sup> architecture that processes  $N$  input points with three-dimensional coordinates through a local self-attention mechanism. The model begins with an input projection that maps the coordinates via  $3 \rightarrow 128 \rightarrow 128$  with Layer Normalization and Rectified Linear Unit activations. The core architecture consists of 12 transformer blocks, each comprising a PointTransformer layer with 16 nearest neighbors and a feed-forward network. The PointTransformer layer computes queries, keys, and values through a shared linear transformation  $128 \rightarrow 384$  (split into three 128-dimensional vectors), and applies position encoding on the relative positions between each point and its  $k$ -nearest neighbors via  $3 \rightarrow 128 \rightarrow 128$  to inject geometric information. Attention weights are computed using a learned transformation on the difference  $\mathbf{q}_i - \mathbf{k}_j + \text{pos}_{ij}$  followed by softmax normalization, and the output is aggregated as a weighted sum of value vectors plus position encodings. Each block includes a feed-forward network with expansion ratio 4 (i.e.,  $128 \rightarrow 512 \rightarrow 128$ ) using Gaussian Error Linear Unit activations, with residual connections and Layer Normalization after both the attention and feed-forward stages. After the transformer blocks, global context is extracted via mean pooling across points, followed by  $128 \rightarrow 128$  projection with Rectified Linear Unit activation, then broadcast and concatenated with local features to form a 256-dimensional per-point representation. The output head applies  $256 \rightarrow 128 \rightarrow 64 \rightarrow 1$  with Layer Normalization, Rectified Linear Unit activations, and dropout probability 0.1, yielding one pressure value per point. Training uses 10,000 points per surface, batch size 8, and 200 epochs with the adaptive moment estimation optimizer (learning rate  $10^{-3}$ , weight decay 0), a one-cycle learning rate schedule, mean squared error loss, gradient clipping with norm 1.0, and validation every epoch.

### **Transolver**

The Transolver model<sup>12</sup> ingests per-point geometric features composed of three-dimensional coordinates and surface normals, forming a six-dimensional feature vector  $[\mathbf{x}, \mathbf{y}, \mathbf{z}, \mathbf{n}_x, \mathbf{n}_y, \mathbf{n}_z]$ . Unified position encoding is disabled, so features are processed directly without additional positional augmentation, yielding a six-dimensional input that is lifted by a multilayer perceptron to a hidden dimension of 256. The network stacks five transformer blocks with eight attention heads each. In every block, a physics-aware attention module for irregular meshes first assigns points to a fixed number of slices (32 per head) using learned soft assignment weights, pools features within each slice to form slice tokens, performs self-attention among slice tokens, and then projects the attended slice information back to points ("deslicing"); this is wrapped with Layer Normalization and a residual connection. A position-wise feed-forward network with Gaussian Error Linear Unit activations and a width expansion ratio of 2 follows, also with Layer Normalization and a residual connection; in the final block, a linear projection produces a single pressure value per point. A learnable global offset vector is added to the hidden representation before the transformer stack, and dropout is set to 0.0. Training uses 10,000 points per surface sample, batch size 64, and 1,000 epochs with the adaptive moment estimation optimizer (learning rate  $10^{-3}$ , weight decay 0), mean squared error loss, a step learning-rate scheduler that decays the rate by a factor of 0.1 every 50 epochs, gradient clipping with norm 1.0, early stopping with patience 50 epochs, validation every 5 epochs, and mixed precision disabled.

### **TransolverLarge**

We evaluate a larger variant of the Transolver model<sup>12</sup> with increased capacity. This enhanced architecture processes point-wise geometric representations consisting of three-dimensional spatial coordinates and surface normal vectors, forming a six-dimensional input feature space  $[\mathbf{x}, \mathbf{y}, \mathbf{z}, \mathbf{n}_x, \mathbf{n}_y, \mathbf{n}_z]$  that is lifted by a multi-layer perceptron to a 384-dimensional hidden representation. The framework employs seven sequential transformer layers, each utilizing twelve parallel attention mechanisms.

Within each layer, a physics-aware attention mechanism for irregular geometric meshes initially distributes points across 48 discrete slices per attention head through learned soft assignment weights computed via Gumbel-Softmax, aggregates information within each slice to form slice-level token representations, executes self-attention computations across these slice tokens, and subsequently redistributes the processed information back to individual points through an inverse slicing operation; this process incorporates Layer Normalization and residual connections. A position-wise feed-forward network follows with Gaussian Error Linear Unit nonlinearities and an expansion factor of 2, also employing Layer Normalization and residual pathways; the terminal layer applies Layer Normalization followed by a linear transformation to generate scalar pressure predictions per point. The hidden representations are augmented with a learnable global placeholder vector prior to transformer processing, while dropout regularization is configured at 0.1. Training uses 10,000 surface points per sample, batch size 1, and 1,000 epochs with the adaptive moment estimation optimizer (learning rate  $10^{-4}$ , no weight regularization), mean squared error loss, step-wise learning rate reduction by factor 0.1 every 150 epochs, gradient norm clipping at 1.0, early termination with 50-epoch patience, and validation assessment every 5 epochs.

### **Transolver++**

The Transolver++ model<sup>13</sup> processes point-wise geometric representations consisting of three-dimensional spatial coordinates and surface normal vectors, forming a six-dimensional input feature space  $[\mathbf{x}, \mathbf{y}, \mathbf{z}, \mathbf{n}_x, \mathbf{n}_y, \mathbf{n}_z]$ . The framework employs five sequential transformer layers, each utilizing eight parallel attention mechanisms. Within each layer, a specialized physics-aware attention mechanism for irregular geometric meshes initially distributes points across 32 discrete slices per attention head through learned soft assignment weights computed via Gumbel-Softmax, aggregates information within each slice to form slice-level token representations, executes self-attention computations across these slice tokens, and subsequently redistributes the processed information back to individual points through an inverse slicing operation; this process incorporates Layer Normalization and residual connections. A position-wise feed-forward network follows with Gaussian Error Linear Unit nonlinearities and an expansion factor of 1, also employing Layer Normalization and residual pathways; the terminal layer applies Layer Normalization followed by a linear transformation to generate scalar pressure predictions per point. The hidden representations are augmented with a trainable global placeholder vector prior to transformer processing, while dropout regularization is set to 0.0. Training uses 10,000 surface points per sample, batch size 8, and 200 epochs with the adaptive moment estimation optimizer (learning rate  $10^{-3}$ , no weight regularization), mean squared error loss, step-wise learning rate reduction by factor 0.1 every 50 epochs, gradient norm clipping at 1.0, early termination with 50-epoch patience, and validation assessment every 5 epochs.

### **TripNet**

The model encodes 3D car geometries into a triplane representation that combines global volumetric context with local spatial resolution<sup>29</sup>. Specifically, the 3D input shape is projected onto three orthogonal feature planes ( $xy$ ,  $yz$ ,  $xz$ ), each represented as a 32-channel latent feature map of size  $128 \times 128$ . These planes are processed independently using a shared U-Net encoder-decoder with residual convolutional blocks, skip connections, and Group Normalization layers, producing refined triplane features that capture multi-scale geometric information. To reconstruct local aerodynamic quantities, query points in 3D space  $(x, y, z)$  are used to bilinearly sample corresponding features from each plane, which are then concatenated and augmented with the spatial coordinates. This concatenated feature vector is passed through a four-layer MLP ( $96 \rightarrow 256 \rightarrow 128 \rightarrow 64 \rightarrow 1$ ) with GELU activations and dropout  $p = 0.1$ , predicting a scalar aerodynamic field value such as surface pressure or velocity component. Training uses  $128^3$  voxelized triplane inputs, a batch size of 4, and 100 epochs, optimized using Adam ( $\text{lr} = 10^{-4}$ , weight decay  $10^{-5}$ ) with a cosine learning rate scheduler and mixed precision. By leveraging implicit neural representations and triplane embeddings, TripNet achieves high-fidelity, spatially continuous predictions while maintaining computational efficiency, effectively bridging volumetric field learning and geometric conditioning for aerodynamic analysis.

### **AB-UPT**

Anchored-Branched Universal Physics Transformers (AB-UPT)<sup>14</sup> are transformer-based neural surrogates. The architecture (i) decouples geometry encoding from field prediction using *multi-branch operators*, improving specialization for complex surface-volume interactions; (ii) achieves scalability by performing neural simulation in a low-dimensional latent space and recovering high-resolution outputs via *anchored neural field decoders*, enabling predictions on meshes with  $3.3 \times 10^4$  to  $1.5 \times 10^8$  cells; and (iii) enforces physics consistency through a *divergence-free* formulation for vector fields (e.g., vorticity). The anchored decoder further permits hard constraint enforcement without degrading performance, and the overall design supports neural simulation directly from CAD geometry, obviating costly CFD meshing at inference time. The authors of AB-UPT<sup>14</sup> kindly provided details about their training setup, reporting a total training duration of 6 hours, 6 minutes, and 51 seconds (including evaluation). The evaluation phase accounted for approximately 25 minutes, resulting in an effective training time of around 5 hours and 40 minutes on a single NVIDIA H100 GPU. To ensure correctness and fair comparison across models, we independently re-ran the evaluation using the same configuration and verified the reported performance on our benchmark pipeline.

### Comparative Architectural Analysis of Transformer Models

Table 7 highlights the key distinctions between the transformer architectures used in the CarBench benchmark. PointTransformer relies on local  $k$ -NN attention with explicit relative position encoding, giving it strong geometric inductive bias but high memory usage due to storing neighborhood graphs. The Transolver family introduces slice-based global attention, which groups tokens into a small number of learnable slices, reducing the quadratic cost of full attention to  $O(NG + G^2d)$ . Transolver++ improves stability and efficiency via temperature-scaled slicing and compact MLPs, achieving the smallest parameter count (1.81M). TransolverLarge expands the capacity (384 channels, 48 slices), yielding higher accuracy at higher cost. AB-UPT employs a hierarchical design with anchor tokens that perform full self-attention and query tokens that interact with anchors only via cross-attention. This structure yields excellent global receptive fields and extremely low memory usage (0.27 GB) while achieving the best predictive accuracy among all models. Together, these models illustrate the progression from local geometric attention (PointTransformer) to global, efficient, and multi-scale mechanisms (Transolver-family) and finally to hierarchical compression (AB-UPT).

**Table 7.** Comparison of transformer-based architectures evaluated on DrivAerNet++ for 3D surface-field prediction. The table summarizes the core attention mechanisms, positional encoding strategies, model scales, and computational complexity of each architecture. Complexity notation:  $N$  = number of surface points;  $k$  = number of nearest neighbors for local attention;  $G$  = number of learnable slices/groups in slice-based attention;  $d$  = hidden feature dimension;  $N_a$  = number of anchor tokens in AB-UPT encoder self-attention;  $N_q$  = number of query tokens in decoder cross-attention. These quantities determine the computational cost of attention operations across different architectural paradigms.

Model	Attention Type	Position Encoding	Dim	Layers	Params (M)	Complexity
<b>PointTransformer</b>	Local $k$ -NN self-attn	Relative offsets $\mathbf{p}_i - \mathbf{p}_j$ (MLP)	128	12	3.05	$O(Nkd)$
<b>Transolver</b>	Slice-based physics attention	Features only (6D)	256	5	2.47	$O(NG + G^2d)$
<b>Transolver++</b>	Slice-based physics attn (Gumbel)	Coord concat (9D)	256	5	1.81	$O(NG + G^2d)$
<b>TransolverLarge</b>	Slice-based attention (scaled-up)	Features only (6D)	384	7	7.58	$O(NG + G^2d)$
<b>AB-UPT</b>	Anchor self-attn + cross-attn	Rotary Positional Embedding (RoPE)	256	12	6.01	$O(N_a^2 + N_q N_a)$

## Navier–Stokes Equations

In this benchmark, the objective is to learn the steady-state pressure distribution  $p(\mathbf{x})$  on the surface of a car, as computed by high-fidelity computational fluid dynamics (CFD) simulations. The underlying physical behavior is governed by the incompressible Navier–Stokes equations:

$$\nabla \cdot \mathbf{u} = 0, \quad (3)$$

$$\rho \left( \frac{\partial \mathbf{u}}{\partial t} + (\mathbf{u} \cdot \nabla) \mathbf{u} \right) = -\nabla p + \mu \nabla^2 \mathbf{u} + \mathbf{f}, \quad (4)$$

where  $\mathbf{u}$  is the velocity vector field,  $p$  the pressure field,  $\rho$  the fluid density,  $\mu$  the dynamic viscosity, and  $\mathbf{f}$  represents external body forces (e.g., gravity). Equation (3) enforces mass conservation, while Equation (4) represents momentum conservation.

To close the system for turbulent flows at high Reynolds numbers typical of automotive applications, we use the Reynolds-Averaged Navier–Stokes (RANS) approach with the  $k$ - $\omega$  Shear Stress Transport (SST) turbulence model<sup>38</sup>. This model solves two additional transport equations for the turbulent kinetic energy  $k$  and the specific dissipation rate  $\omega$ :

$$\frac{\partial(\rho k)}{\partial t} + \nabla \cdot (\rho k \mathbf{u}) = P_k - \beta^* \rho k \omega + \nabla \cdot [(\mu + \sigma_k \mu_t) \nabla k], \quad (5)$$

$$\begin{aligned} \frac{\partial(\rho \omega)}{\partial t} + \nabla \cdot (\rho \omega \mathbf{u}) &= \alpha \frac{\omega}{k} P_k - \beta \rho \omega^2 + \nabla \cdot [(\mu + \sigma_\omega \mu_t) \nabla \omega] \\ &+ 2(1 - F_1) \rho \sigma_{\omega 2} \frac{1}{\omega} \nabla k \cdot \nabla \omega. \end{aligned} \quad (6)$$

Here  $P_k$  denotes the production of turbulent kinetic energy and  $\mu_t$  is the eddy viscosity defined as  $\mu_t = \rho k / \omega$ . The SST model blends the standard  $k$ - $\omega$  model near the wall with the  $k$ - $\varepsilon$  model in the freestream, improving accuracy for adverse pressure gradients and separation.

By taking the divergence of the momentum equation (4) and using the continuity constraint (3), we obtain the pressure Poisson equation:

$$\nabla^2 p = \rho \nabla \cdot [(\mathbf{u} \cdot \nabla) \mathbf{u}] + \nabla \cdot \mathbf{f}. \quad (7)$$

This equation reveals that the pressure field arises from the spatial acceleration of the flow and any applied forces. In our learning task, the surrogate models aim to approximate this surface pressure field directly from the car geometry, bypassing the need for solving the full Navier–Stokes system during inference. The pressure field on the car surface emerges from the solution to the momentum equation and is influenced by velocity gradients and turbulence-induced stresses. In regions with complex flow separation, curvature, or underbody vortices, the accurate prediction of surface pressure becomes a challenging task. Our deep learning models aim to learn the nonlinear mapping from surface geometry to the pressure distribution without explicitly solving the above PDE system.

### Pressure Drag and Its Role in Automotive Aerodynamics

The total aerodynamic drag  $D$  experienced by a car moving through air can be decomposed into two primary components:

$$D = D_p + D_f, \quad (8)$$

where

- $D_p$  is the pressure drag (form drag),
- $D_f$  is the friction drag (skin-friction drag due to shear stresses).

Pressure drag arises from the imbalance between the high pressure at the front of the car and the low pressure in the wake region at the rear. It is computed by integrating the surface pressure over the body in the streamwise direction. Using the outward surface normal  $\mathbf{n}$  and freestream direction  $\hat{\mathbf{x}}$ , the pressure drag can be expressed as

$$D_p = - \int_A (p(\mathbf{x}) - p_\infty) \mathbf{n} \cdot \hat{\mathbf{x}} dA, \quad (9)$$

where

- $A$  is the car surface (projected frontal) area,

- $\mathbf{n}$  is the outward surface normal vector,
- $\hat{\mathbf{x}}$  is the unit vector in the freestream (drag) direction,
- $p_\infty$  is the freestream static pressure.

In contrast, friction drag is computed from the wall shear stress vector  $\boldsymbol{\tau}_w$ :

$$D_f = \int_A \boldsymbol{\tau}_w \cdot \hat{\mathbf{x}} dA, \quad \boldsymbol{\tau}_w = \mu \left. \frac{\partial \mathbf{u}_t}{\partial n} \right|_w, \quad (10)$$

where  $\mathbf{u}_t$  is the tangential velocity at the wall and  $n$  is the wall-normal direction.

The dimensionless drag coefficient  $C_D$  is defined as

$$C_D = \frac{D}{\frac{1}{2} \rho U_\infty^2 A_{\text{ref}}}, \quad (11)$$

where  $U_\infty$  is the freestream velocity and  $A_{\text{ref}}$  is the frontal area of the car.

For streamlined cars, friction drag can be significant; however, in typical passenger cars with bluff geometries and separated wakes, pressure drag is often the dominant contributor, accounting for up to 80–90%<sup>22,23</sup> of the total drag. Therefore, accurately learning and predicting the surface pressure distribution is critical for estimating and optimizing aerodynamic performance.

### **Relevance of Pressure Distribution to Aeroacoustics**

In addition to its critical role in aerodynamic drag, the pressure field around a car also contributes significantly to aerodynamic noise generation, particularly at high speeds. This phenomenon, known as aeroacoustic noise, originates from unsteady pressure fluctuations associated with turbulent flows, separations, wakes, and vortices.

One of the key frameworks in aeroacoustics is Lighthill's acoustic analogy<sup>53</sup>, which describes the generation of sound due to turbulence:

$$\frac{\partial^2 \rho'}{\partial t^2} - c_0^2 \nabla^2 \rho' = \frac{\partial^2 T_{ij}}{\partial x_i \partial x_j}, \quad (12)$$

where

- $\rho'$  is the acoustic density fluctuation,
- $c_0$  is the speed of sound,
- $T_{ij}$  is Lighthill's stress tensor:

$$T_{ij} = \rho u_i u_j + [(p - c_0^2 \rho) \delta_{ij} - \tau_{ij}],$$

- $\tau_{ij}$  is the viscous stress tensor.

The dominant aerodynamic noise sources in cars arise from turbulent boundary layers forming over mirrors and A-pillars, flow separation at the rear, and vortex shedding in the wheel arches and underbody regions<sup>54</sup>. These localized and rapid pressure fluctuations, particularly in the near-wake, generate broadband acoustic emissions that contribute significantly to overall car noise. Consequently, accurately learning and predicting the surface pressure distribution is essential not only for estimating drag but also for identifying acoustic hot spots, predicting noise radiation patterns, and enabling design optimization to minimize flow-induced noise.